Cosmic evolution of the C IV in high-resolution hydrodynamic simulations

E. Tescari,[1,2,3]⋆ M. Viel,[1,2] V. D'Odorico,[1] S. Cristiani,[1,2] F. Calura,[1,4] S. Borgani[1,2,3] and L. Tornatore[1,2,3]

[1]*INAF - Osservatorio Astronomico di Trieste, Via G.B. Tiepolo 11, I-34131 Trieste, Italy*
[2]*INFN/National Institute for Nuclear Physics, Via Valerio 2, I-34127 Trieste, Italy*
[3]*Dipartimento di Fisica - Sezione di Astronomia, Università di Trieste, Via G.B. Tiepolo 11, I-34131 Trieste, Italy*
[4]*Jeremiah Horrocks Institute for Astrophysics and Supercomputing, University of Central Lancashire, Preston PR1 2HE*

ABSTRACT

We investigate the properties of triply ionized carbon (C IV) in the intergalactic medium (IGM) using a set of high resolution and large box size cosmological hydrodynamic simulations of a Lambda cold dark matter (ΛCDM) model. We rely on a modification of the publicly available TreeSPH code GADGET-2 that self-consistently follows the metal enrichment mechanism by means of a detailed chemical evolution model. We focus on several numerical implementations of galactic feedback: galactic winds in the energy-driven and momentum-driven prescriptions, galactic winds hydrodynamically coupled to the surrounding gas and active galactic nuclei (AGNs) powered by gas accretion on to massive black holes. Furthermore, our results are compared to a run in which galactic feedback is not present and we also explore different initial stellar mass function. After having addressed some global properties of the simulated volume like the impact on the star formation rate and the content in carbon and C IV, we extract mock IGM transmission spectra in neutral hydrogen (H I) and C IV and perform Voigt profile fitting. The results are then compared with high-resolution quasar (QSO) spectra obtained with the Ultraviolet Echelle Spectrograph (UVES) at the Very Large Telescope (VLT) and the High Resolution Echelle Spectrograph (HIRES) at Keck. We find that feedback has little impact on statistics related to the neutral hydrogen, while C IV is more affected by galactic winds and/or AGN feedback. The feedback schemes investigated have a different strength and redshift evolution with a general tendency for AGN feedback to be more effective at lower redshift than galactic winds. When the same analysis is performed over observed and simulated C IV lines, we find a reasonably good agreement between data and simulations over the column density range $N_{C IV} = 10^{12.5-15}\,\mathrm{cm}^{-2}$. Also the C IV linewidth distribution appears to be in agreement with the observed values, while the H I Doppler parameters, $b_{H I}$, are in general too large, showing that the diffuse cosmic web is heated more than what is inferred by observations. The simulation without feedback fails in reproducing the C IV systems at high column densities at all redshift, while the AGN feedback case agrees with observations only at $z < 3$, when this form of feedback is particularly effective. We also present scatter plots in the b–N and in the $N_{C IV}$–$N_{H I}$ planes, showing that there is rough agreement between observations and simulations only when feedback is taken into account.

Although it seems difficult to constrain the nature and the strength of galactic feedback using the present framework and find a unique model that fits all the observations, these simulations offer the perspective of understanding the galaxy–IGM interplay and how metals produced by stars can reach the low-density IGM.

Key words: methods: numerical – galaxies: formation – intergalactic medium – quasars: absorption lines – cosmology: theory.

1 INTRODUCTION

The interplay between galaxies and the intergalactic medium (IGM) is a fundamental and poorly understood aspect in the standard

⋆E-mail: tescari@oats.inaf.it

scenario of structure formation. The intimate connection between the diffuse IGM and the baryons that populate star-forming galaxies can shed light on the metal enrichment of the IGM (its nature and redshift evolution), on the properties of galactic feedback and on the evolution of the ultraviolet (UV) background.

In recent years, this field has benefitted from spectroscopical observations of quasar (QSO) and gamma-ray burst (GRB) spectra (both at high and low resolution) and from photometric and spectroscopical information on high-redshift galaxies in the same field of view. This has in turn allowed us to perform cross-correlation studies of absorption lines and properties of galaxies (e.g. Steidel et al. 2010, and references therein). Observations have revealed that the IGM is polluted with heavy elements such as carbon, oxygen and silicon (e.g. Weymann, Carswell & Smith 1981; Cowie et al. 1995; Aguirre et al. 2005). Furthermore, high-redshift star-forming galaxies have been shown to interact with the surrounding medium by powering strong galactic outflows (e.g. Adelberger et al. 2005). The IGM enrichment mechanism is, however, still poorly constrained and the extent of metal pollution of the low-density IGM, or around Lyman-break galaxies, controversial (e.g. Schaye et al. 2000a; Porciani & Madau 2005; Pieri, Schaye & Aguirre 2006).

Among many different metal species, the doublet produced by triply ionized carbon (C IV) is the one that has been most widely studied since it is relatively easy to identify in the regions redwards of Lyman α emission. C IV has been observed from low redshift up to very high redshift (Ryan-Weber, Pettini & Madau 2006; Becker, Rauch & Sargent 2009; Ryan-Weber et al. 2009); its clustering properties in the transverse direction and along the line of sight (LOS) have been investigated (D'Odorico, Petitjean & Cristiani 2002; Pichon et al. 2003; Tytler et al. 2009) along with the global evolution of the C IV density fraction down to $z < 2$ (D'Odorico et al. 2010); the optical depth in C IV has been derived using pixel optical depth techniques applied to the Ultraviolet Echelle Spectrograph (UVES) Large Programme (LP) sample in order to constrain the metallicity of the low-density gas (Schaye et al. 2003; Aracil et al. 2004); the cross-correlation between galaxies and C IV properties has also been addressed in great detail using either Keck or UVES spectra (Scannapieco et al. 2006; Simcoe et al. 2006). The general conclusion is that C IV absorption systems are indeed related to outskirts of galactic haloes, but it is still unclear whether the gas producing the absorption is enriched by nearby galaxies or at an earlier epoch by smaller objects.

The large amount of data available has prompted the implementation of relevant physical processes into sophisticated hydrodynamic codes in order to simulate both galaxies and QSO/GRB absorption lines. The first attempt to model C IV properties using hydrodynamic simulations has been made by Haehnelt, Steinmetz & Rauch (1996). Subsequently, it has been demonstrated that a key ingredient that appears to be necessary in order to reproduce C IV metal line statistics is feedback in the form of galactic winds (Theuns et al. 2002; Cen, Nagamine & Ostriker 2005; Oppenheimer & Davé 2006, 2008). Galactic winds triggered by supernovae (SNe) explosions have been modelled in a simple way using mainly two schemes that conserve either energy or momentum (Oppenheimer & Davé 2006; Tescari et al. 2009). Other sources of feedback like active galactic nuclei (AGNs) have also been considered to address global gas properties from high to low redshift (Tornatore et al. 2010). A second very important ingredient has been the implementation of accurate chemical evolution models that self-consistently follow the release of different metal species from stars and also allow for different initial stellar mass functions (Kawata & Rauch 2007; Kobayashi, Springel & White 2007; Tornatore et al. 2007;

Sommer-Larsen & Fynbo 2008; Oppenheimer, Davé & Finlator 2009; Wiersma et al. 2009; Cen & Chisari 2010; Davé et al. 2010; Wiersma et al. 2010).

This is a second paper in a series that exploits the capabilities of a state-of-the-art modification of the publicly available code GADGET-2 (Springel 2005). In the first paper, we addressed neutral hydrogen properties (Tescari et al. 2009) focusing in particular on Damped Lyman α systems. In this paper, we study the C IV transition by extending the feedback models simulated.

This paper is organized as follows. In Sections 2 and 3 we present, respectively, the observational data sample and our set of simulations along with the different feedback models implemented in our code. In Section 4 we compare some global properties of the simulations: the cosmic star formation rate (SFR) and the evolution of the total carbon content. We then focus on the neutral hydrogen statistics in Section 5. In Sections 6 and 7 we investigate the C IV column density distribution function (CDDF) and the evolution with redshift of the C IV cosmological mass density, $\Omega_{C IV}$, respectively. In Section 8 we study the probability distribution function of the C IV Doppler parameter and, in Section 9, we present the C IV column density–Doppler parameter relation. The last part of the paper is dedicated to the analysis of the H I–C IV correlated absorption (Section 10). Finally, in Section 11 we summarize our main results and we draw some conclusions.

2 OBSERVATIONAL DATA SAMPLE

The core of the observational data sample is formed by the high resolution ($R \sim 45\,000$), high signal-to-noise ratio (S/N) QSO spectra obtained with the UVES spectrograph (Dekker et al. 2000) at the Kueyen unit of the European Southern Observatory (ESO) VLT (Cerro Paranal, Chile) in the framework of the ESO LP: 'The Cosmic Evolution of the IGM' (Bergeron et al. 2004).

We have used the sample of H I Lyman α absorption lines described in Saitta et al. (2008) and D'Odorico et al. (2008), which is based on 18 objects of the LP plus four more QSOs, of which J2233−606 and HE1122−1648 were observed with UVES, while HS1946+7658 and B1422+231 were obtained with the HIRES spectrograph at the Keck Telescope at comparable resolution and S/N. In this work, also the H I Lyman α list of the QSO Q0055−269, observed with UVES, has been added to the sample. The adopted sample of C IV absorptions was described in D'Odorico et al. (2010). The previous group of QSOs was increased with the addition of the UVES spectra of PKS2000−330 and PKS1937−101 to extend the redshift interval to $z \gtrsim 3$.

All UVES spectra were reduced with the UVES pipeline following the standard procedure. The continuum level was determined by interpolating with a cubic spline the region of the spectrum free from evident absorption features. Absorption lines were fitted with Voigt profiles using the context LYMAN of the MIDAS reduction package (Fontana & Ballester 1995). A minimum number of components was adopted to fit the velocity profile in order to reach a normalized $\chi^2 \sim 1$. For all the QSOs in the sample, the Lyman α forest was defined as the interval between the Lyman β emission plus $1000\,\mathrm{km\,s^{-1}}$ (to avoid contamination from the Lyman β forest) and $5000\,\mathrm{km\,s^{-1}}$ from the Lyman α emission; the C IV forest was defined as the interval between the Lyman α emission and $5000\,\mathrm{km\,s^{-1}}$ from the C IV emission. The higher bound was fixed to avoid the proximity region affected by the QSO emission, where most of the intrinsic systems are found.

C IV features are distinguished into *components* or *lines*, meaning the velocity components in which every absorption profile has been

decomposed, and *systems*, formed by groups of components with relative separation smaller than $dv_{min} = 50 \, km \, s^{-1}$ (see D'Odorico et al. 2010, for a detailed description of the procedure). Both the velocity components and the systems in the sample have column densities in the range $10^{11} \lesssim N_{C\,IV} \lesssim 10^{15} \, cm^{-2}$.

In order to further increase the number of C IV lines and to extend the sample to higher redshift, D'Odorico et al. (2010) have considered the C IV lines fitted in nine QSO spectra observed with HIRES at Keck at a resolution and S/N similar to those of their spectra and reported in Boksenberg, Sargent & Rauch (2003). The fit with Voigt profiles was carried out by Boksenberg et al. (2003) with VPFIT.[1] The main difference between LYMAN and VPFIT is that the number of components fitted to a given velocity profile is, in general, larger using the latter (see also the discussion in Saitta et al. 2008). This is seen also in the analysis of D'Odorico et al. (2010), in particular from the comparison of the C IV lines detected in the spectrum of the QSO B1422+231, which is the only object in common between the two samples. D'Odorico et al. (2010) find that in all cases the number of components determined with VPFIT is larger or equal to that determined with LYMAN. However, when the total column density of each absorption system is considered the difference between the two fitting procedures becomes negligible.

All the QSOs of the observational sample are reported in Table 1 with their emission redshift and the redshift range covered by the Lyman α forest and the C IV lines.

3 THE SIMULATIONS

In the following we review the main characteristics of the runs analysed in this work and we refer to Tescari et al. (2009) for a more extensive description of the simulations. Our code is the same modified version of the TreePM-SPH code GADGET-2 (Springel 2005) used in Tescari et al. (2009).

The simulations cover a cosmological volume (with periodic boundary conditions) filled with an equal number of dark matter and gas particles. The cosmological model chosen is a flat Lambda cold dark matter (ΛCDM) with the following parameters: $\Omega_{0m} = 0.24$, $\Omega_{0b} = 0.0413$, $\Omega_\Lambda = 0.76$, $n_s = 0.96$, $H_0 = 73 \, km \, s^{-1} \, Mpc^{-1}$ and $\sigma_8 = 0.8$, which are in agreement with the latest results from large-scale structure observables such as the cosmic microwave background, weak lensing, the Lyman α forest and the evolution of mass function of galaxy clusters (Lesgourgues et al. 2007; Komatsu et al. 2009; Vikhlinin et al. 2009). The input linear dark matter power spectrum for the initial conditions has been generated at $z = 99$ with CMBFAST (Seljak & Zaldarriaga 1996) and includes baryonic acoustic oscillations.

Radiative cooling and heating processes are modelled following the implementation of Katz, Weinberg & Hernquist (1996). We assume a mean Ultraviolet Background (UVB) produced by quasars and galaxies as given by Haardt & Madau (1996), with the heating rates multiplied by a factor of 3.3 in order to better fit observational constraints on the temperature evolution of the IGM at high redshift (the factor of 3.3 was originally introduced because it gives a temperature at the mean cosmic density, T_0, in agreement with the Schaye et al. 2000b, data points). This background gives naturally $\Gamma_{-12} \sim 0.8$–1 at low redshift, in agreement with recent observational measurements (Bolton et al. 2005; Faucher-Giguère et al. 2008). Multiplying the heating rates by the factor above (chosen

Table 1. Relevant properties of the QSOs forming the D'Odorico et al. (2010) observational sample.

QSO	z_{em}	$\Delta z_{Ly\alpha}$	$\Delta z_{C\,IV}$
HE 1341−1020	2.142	1.6599–2.090	1.467–2.090
Q0122−380	2.2004	1.709–2.147	1.513–2.147
PKS 1448−232	2.224	1.729–2.171	1.531–2.171
PKS 0237−23	2.233	1.737–2.179	1.538–2.179
J2233-606	2.248	1.7496–2.194	1.550–2.194
HE 0001−2340	2.265	1.764–2.211	1.564–2.211
HS 1626+6433[a]	2.32		1.607–2.265
HE 1122−1648[b]	2.40	1.878–2.344	1.665–2.344
Q0109−3518	2.4057	1.883–2.349	1.674–2.349
HE 2217−2818	2.414	1.888–2.355	1.681–2.355
Q0329−385	2.435	1.9096–2.378	1.697–2.378
HE 1158−1843	2.448	1.919–2.391	1.707–2.391
HE 1347−2457	2.5986	2.046–2.539	1.826–2.539
Q1442+2931[a]	2.661		1.875–2.600
Q0453−423	2.669	2.106–2.608	1.881–2.608
PKS 0329−255	2.696	2.129–2.635	1.902–2.635
HE 0151−4326	2.763	2.186–2.701	1.955–2.701
Q0002−422	2.769	2.191–2.707	1.959–2.707
HE 2347−4342	2.880	2.285–2.816	2.067–2.816
SBS 1107+487[a]	2.966		2.114–2.900
HS 1946+7658[c]	3.058	2.435–2.991	2.181–2.991
HE 0940−1050	3.0932	2.465–3.025	2.214–3.025
Q0420−388	3.1257	2.493–3.057	2.239–3.057
S4 0636+68[a]	3.175		2.278–3.106
SBS 1425+606[a]	3.199		2.297–3.129
PKS 2126−158	3.292	2.633–3.221	2.370–3.221
B1422+231[b]	3.623	2.914–3.546	2.630–3.546
Q0055−269	3.66	2.945–3.583	2.659–3.583
PKS 2000−330	3.783		2.756–3.704
PKS 1937−101	3.787		2.770–3.400
PSS J1646+5514[a]	4.059		2.972–3.975
PSS J1057+4555[a]	4.131		3.029–4.046
BR 2237−0607[a]	4.559		3.365–4.467

[a]QSOs from Boksenberg et al. (2003).
[b]Reduced spectra kindly provided by T.-S. Kim.
[c]Data from Kirkman & Tytler (1997).

empirically) results in a larger IGM temperature at the mean density which cannot be reached by the standard hydrodynamic code. This aims at mimicking, at least in a phenomenological way, the non-equilibrium ionization effects around reionization (see for example Ricotti, Gnedin & Shull 2000; Schaye et al. 2000a; Bolton & Haehnelt 2007). A significant fraction in mass of the IGM resides in the tight power-law relation $T = T_0(1 + \delta)^{\gamma-1}$ at around the mean density, where T_0 is the temperature at the mean cosmic density and δ the overdensity. Our reference simulations (see at the end of this Section) at redshift $z = 3$, 2.25 and 1.5 have $\log\langle T_0(K)\rangle$, respectively, equal to 4.36, 4.33, 4.30, and γ, respectively, equal to 1.58, 1.60, 1.62.

In our simulations, the standard multiphase star formation criterion of Springel & Hernquist (2003) is implemented, which contains an effective prescription for the interstellar medium (ISM). In this effective model, whenever the density of a gas particle exceeds a given threshold (set to $\rho_{th} = 0.1 \, cm^{-3}$ in terms of the number density of hydrogen atoms), that gas particle is flagged as star forming and is treated as multiphase. With this prescription, baryons are in the form of either a hot or a cold phase or in stars, thereby this density threshold marks the onset of cold clouds formation.

We follow self-consistently the evolution of these elements: H, He, C, O, Mg, S, Si and Fe. The contribution of metals is included in

---

[1] http://www.ast.cam.ac.uk/~rfc/vpfit.html

the cooling function using the tables of Sutherland & Dopita (1993) that assume the solar value for the relative abundances. In this paper we use the solar metallicity and element abundances given by Asplund, Grevesse & Sauval (2005), with $Z/X = 0.0165$. Besides including different contributions from Type II and Type Ia supernovae (SNeII and SNeIa, respectively) and low- and intermediate-mass stars (LIMS), our model of chemical evolution accounts for mass-dependent stellar lifetimes. We adopt the lifetime function given by Padovani & Matteucci (1993). We use these stellar yields: Thielemann et al. (2003) for the SNeIa, Woosley & Weaver (1995) for the SNeII and van den Hoek & Groenewegen for the LIMS. The mass range for the SNeII is $m > 8\,M_\odot$, while for the SNeIa $m < 8\,M_\odot$ with a binary fraction of 10 per cent. Finally, we use three distinct stellar initial mass functions (IMFs): a Kroupa, a Salpeter and an Arimoto–Yoshii IMFs. For this paper, our reference choice is the Kroupa IMF (Kroupa 2001), which consists of a multislope approximation: $y_{KR} = 0.3$ for stellar mass $m < 0.5\,M_\odot$, $y_{KR} = 1.2$ for $0.5\,M_\odot \leq m < 1\,M_\odot$ and $y_{KR} = 1.7$ for $m \geq 1\,M_\odot$ (where $\varphi(m) \propto m^{-y}$ is the functional form for the IMF and $\varphi(m)$ is the IMF by mass). Salpeter (Salpeter 1955) IMF has single slope $y_{SL} = 1.35$ and Arimoto–Yoshii (Arimoto & Yoshii 1987) IMF also has single slope $y_{AY} = 0.95$.

In this paper, we use three different feedback schemes: two associated to the galactic (energy and momentum driven) winds produced by 'starburst' galaxies, already presented in Tescari et al. (2009) and the (new) AGN feedback associated to the energy released by gas accretion on to supermassive black holes (BHs). In the following we briefly describe these different models.

3.1 Energy-driven winds (EDW)

For this implementation, the wind mass-loss rate $\dot{M}_w$ is assumed to be proportional to the SFR $\dot{M}_\star$ according to

$$\dot{M}_w = \eta \dot{M}_\star, \tag{1}$$

where η is the wind mass loading factor (i.e. the wind efficiency) and the wind carries a fixed fraction χ of SN energy:

$$\frac{1}{2} \dot{M}_w v_w^2 = \chi \epsilon_{SN} \dot{M}_\star. \tag{2}$$

Star-forming gas particles are then stochastically selected according to their SFR to become part of a blowing wind. Whenever a particle is uploaded to the wind, it is decoupled from the hydrodynamics for a given period of time or till the density around it drops below a given fraction of the density threshold for the onset of the star formation ($\rho_{th} = 0.1\,cm^{-3}$ in terms of the number density of hydrogen atoms), in order to effectively reach less 'dense regions'. The (lower) limiting density for decoupling is set to $0.5\rho_{th}$. This allows the wind particle to travel 'freely' up to few kpc until it has left the dense star-forming phase, without directly interacting with it. Otherwise, to verify the effect of the decoupling, we run a 'coupled winds' simulation in which wind particles are always affected by the hydrodynamics like all the other gas particles (see also Dalla Vecchia & Schaye 2008; Tornatore et al. 2010). Unlike in Springel & Hernquist (2003), we fixed the velocity of the winds, v_w, instead of the fraction of the energy made available by SNeII explosions to power galactic ejecta. Thus, four parameters fully specify the wind model: the wind efficiency η, the wind speed v_w, the wind free travel length l_w and the wind free travel density factor δ_w. The maximum allowed time for a wind particle to stay hydrodynamically decoupled is then $t_{dec} = l_w/v_w$ (note that in the case of coupled winds $t_{dec} = 0$). The parameter l_w has been introduced in order to prevent a gas particle from being trapped into the potential well of the virialized halo and in order to effectively escape from the ISM, reach the low-density IGM and pollute it with metals.

In this paper, we use $l_w = 10\,h^{-1}\,kpc$ and we considered two different values for the wind velocity: $v_w = 300$ and $500\,km\,s^{-1}$. In our implementation, the parameter η is kept fixed to the value 2.

3.2 Momentum-driven winds (MDW)

A feasible physical scenario for the wind-driving mechanism, outlined by Murray, Quataert & Thompson (2005) to explain observational evidence of outflows from starburst galaxies (Martin 2005; Rupke, Veilleux & Sanders 2005), is the so-called momentum-driven wind model. In this scenario, the radiation pressure of the starburst drives an outflow, possibly by transferring momentum to an absorptive component (e.g. dust) that is hydrodynamically coupled with the gas component, which is then dragged out of the galaxy. Following Oppenheimer & Davé (2006, 2008), we implemented the MDW model in our code. In such a model the wind speed scales as the galaxy velocity dispersion σ, as observed by Martin (2005). Since in MDW the amount of input momentum per unit star formation is constant, this implies that the wind mass loading factor η must be inversely proportional to the velocity dispersion. We therefore use the following relations:

$$v_{wind} = 3\sigma \sqrt{f_L - 1}; \quad \eta = \frac{\sigma_0}{\sigma}, \tag{3}$$

where f_L is the luminosity factor in units of the galactic Eddington luminosity (i.e. the critical luminosity necessary to expel gas from the galaxy), σ_0 is the normalization of the mass loading factor and we add an extra 2σ kick to get out of the potential of the galaxy in order to simulate continuous pumping of gas until it is well into the galactic halo. To determine σ, we identify haloes runtime in the simulations by using a parallel friends-of-friends (FoF) algorithm and we associate σ with the velocity dispersion of the haloes, σ_{DM} (for further details see section 2.2 of Tescari et al. 2009). Schaerer (2003) suggested an approximate functional form for far-UV emission which Oppenheimer & Davé (2006, 2008) used to obtain the luminosity factor and which includes a metallicity dependence for f_L, owing to more UV photons output by lower metallicity stellar populations:

$$f_L = f_{L_\odot} \times 10^{-0.0029(\log Z + 9)^{2.5} + 0.417694}, \tag{4}$$

where Martin (2005) suggests $f_{L_\odot} \approx 2$. The mass loading factor controls star formation at early times, so σ_0 can also be set by requiring a match to the observed global SFR. Following Oppenheimer & Davé (2006, 2008), we set $\sigma_0 = 150\,km\,s^{-1}$. Even for this wind implementation, the particles are stochastically selected in the same way as for the energy-driven scenario.

3.3 AGN feedback

Finally, we include in our simulations the effect of feedback energy from gas accretion on to super-massive BHs, following the scheme originally introduced by Springel, Di Matteo & Hernquist (2005) (see also Di Matteo, Springel & Hernquist 2005). In this model, BHs are represented by collisionless sink particles initially seeded in dark matter haloes, which subsequently grow via gas accretion and through mergers with other BHs during close encounters. Every new dark matter halo, identified by a run-time FoF algorithm above the mass threshold $M_{th} = 10^{10}\,M_\odot$, is seeded with a central BH of initial mass $10^5\,M_\odot$, provided the halo does not contain any BHs

Table 2. Summary of the different runs. Columns are as follows: (1) run name; (2) IMF chosen; (3) comoving box size; (4) number of gas particles; (5) mass of gas particle; (6) Plummer-equivalent comoving gravitational softening and (7) type of feedback implemented. For the runs kr37edw500, kr37co-edw500, ay37edw500, sa37edw500 and kr37p400edw500, the velocity of the EDW is set to $v_w = 500\,\mathrm{km\,s^{-1}}$.

Run	IMF	Box size $[h^{-1}\,\mathrm{Mpc}]$	N_{GAS}	m_{GAS} $[h^{-1}\,\mathrm{M_\odot}]$	Softening $[h^{-1}\,\mathrm{kpc}]$	Feedback
kr37edw500	Kroupa	37.5	256^3	3.6×10^7	7.5	EDW
kr37mdw	Kroupa	37.5	256^3	3.6×10^7	7.5	MDW[a]
kr37agn	Kroupa	37.5	256^3	3.6×10^7	7.5	AGN[b]
kr37agn+edw300	Kroupa	37.5	256^3	3.6×10^7	7.5	AGN+EDW[c]
kr37nf	Kroupa	37.5	256^3	3.6×10^7	7.5	No feedback
kr37co-edw500	Kroupa	37.5	256^3	3.6×10^7	7.5	Coupled EDW[d]
ay37edw500	Arimoto–Yoshii	37.5	256^3	3.6×10^7	7.5	EDW
sa37edw500	Salpeter	37.5	256^3	3.6×10^7	7.5	EDW
kr37p400edw500	Kroupa	37.5	400^3	9.4×10^6	4.8	EDW

[a]MDW feedback in which wind velocity scales roughly with 3σ (σ being the velocity dispersion of the halo that hosts the 'wind' particle).
[b]AGN feedback in which the energy is released by gas accretion on to supermassive BHs.
[c]Combined effect of EDW of $300\,\mathrm{km\,s^{-1}}$ and AGN feedbacks.
[d]EDW not decoupled from the hydrodynamics (see Section 3.1).

yet. Each BH can then grow by local gas accretion, with a rate given by

$$\dot{M}_{\mathrm{BH}} = \min\left(\dot{M}_{\mathrm{B}}, \dot{M}_{\mathrm{Edd}}\right), \tag{5}$$

where $\dot{M}_{\mathrm{B}}$ is the accretion rate estimated with the Bondi–Hoyle–Littleton formula (e.g. Bondi 1952) and $\dot{M}_{\mathrm{Edd}}$ is the Eddington accretion rate. We refer to Springel et al. (2005) for the details of the AGN feedback implementation and to Booth & Schaye (2009) for a review of the BH accretion feedback in the context of cosmological simulations. An important parameter of the model is the radiative efficiency, ϵ_{r}, which gives the radiated energy L_{r} in units of the energy associated to the accreted mass:

$$\epsilon_{\mathrm{r}} = \frac{L_{\mathrm{r}}}{\dot{M}_{\mathrm{BH}}c^2}. \tag{6}$$

Following Springel et al. (2005) and Fabjan et al. (2010), we fix $\epsilon_{\mathrm{r}} = 0.1$ as a reference value, which is typical for a radiatively efficient accretion on to a Schwarzschild BH (Shakura & Sunyaev 1973). The model then assumes that a fraction ϵ_{f} of the radiated energy is thermally coupled to the surrounding gas, so that $\dot{E}_{\mathrm{feed}} = \epsilon_{\mathrm{r}}\epsilon_{\mathrm{f}}\dot{M}_{\mathrm{BH}}c^2$ is the rate of the energy released to heat the surrounding gas. Using $\epsilon_{\mathrm{f}} \sim 0.05$, Di Matteo et al. (2005) were able to reproduce the observed M_{BH}–σ relation between bulge velocity dispersion and mass of the hosted BH (see also Di Matteo et al. 2008; Sijacki et al. 2008). Gas particle accretion on to the BH is implemented in a stochastic way by assigning to each neighbouring gas particle a probability of contributing to the accretion, which is proportional to the smoothed particle hydrodynamics (SPH) kernel weight computed at the particle position. In the scheme described above, this stochastic accretion is used only to increase the dynamic mass of the BHs, while the mass entering in the computation of the accretion rate is followed in a continuous way by integrating the analytic expression for $\dot{M}_{\mathrm{BH}}$. Once the amount of energy to be thermalized is computed for each BH at a given time-step, this energy is then distributed to the surrounding gas particles using the SPH kernel weighting scheme.

Our research group explored for the first time this new feedback prescription in relation to the high-redshift properties of the IGM, while Tornatore et al. (2010) have studied the impact of this feedback mechanism on the low-redshift IGM (other groups are working

on the BH accretion feedback related to IGM and the warm hot intergalactic medium (WHIM); see for example Wiersma et al. 2010; Bertone et al. 2010a,b).

In Table 2 we summarize the main parameters of the cosmological simulations performed, including the mass associated to the gas particles and the gravitational softening. All the simulations start at redshift $z = 99$ and stop at redshift $z = 1.5$. In the following, we outline the specific characteristics of each run.

(i) kr37edw500: EDW of velocity $v_w = 500\,\mathrm{km\,s^{-1}}$ and Kroupa IMF (the reference IMF for this work).

(ii) kr37mdw: MDW and Kroupa IMF.

(iii) kr37agn: in this simulation the AGN feedback mechanism, associated to the energy released by gas accretion on to supermassive BHs and described in Section 3.3, is active.

(iv) kr37agn+edw300: in this simulation two different feedback models are combined: the energy-driven galactic winds of velocity $v_w = 300\,\mathrm{km\,s^{-1}}$ and the AGN feedback. We will see that this run is completely different from the kr37agn simulation mentioned above. In fact, the galactic winds start to be effective at a higher redshift than the AGN feedback, making the haloes devoid of gas and consequently reducing the efficiency of the BH accretion and the power of the AGN feedback. Therefore, the effect of the winds is more prominent than that of the AGN, with the result that the kr37agn+edw300 run behaves very similarly to a regular EDW simulation.

(v) kr37nf: this simulation was run without any winds or AGN feedback in order to test how large the effects of the different feedback prescriptions on the C IV statistics are.

(vi) kr37co-edw500: as we stated in Section 3.1, this simulation has EDW of velocity $v_w = 500\,\mathrm{km\,s^{-1}}$, never decoupled from the hydrodynamics. We will show that the coupled winds result in a less efficient feedback with respect to the original implementation.

(vii) ay37edw500: EDW of velocity $v_w = 500\,\mathrm{km\,s^{-1}}$ and Arimoto–Yoshii IMF.

(viii) sa37edw500: EDW of velocity $v_w = 500\,\mathrm{km\,s^{-1}}$ and Salpeter IMF (runs kr37edw500, ay37edw500 and sa37edw500 are identical, except for the IMF).

(ix) kr37p400edw500: EDW of velocity $v_w = 500\,\mathrm{km\,s^{-1}}$ and Kroupa IMF, with a number of particles (gas + dark matter) equal
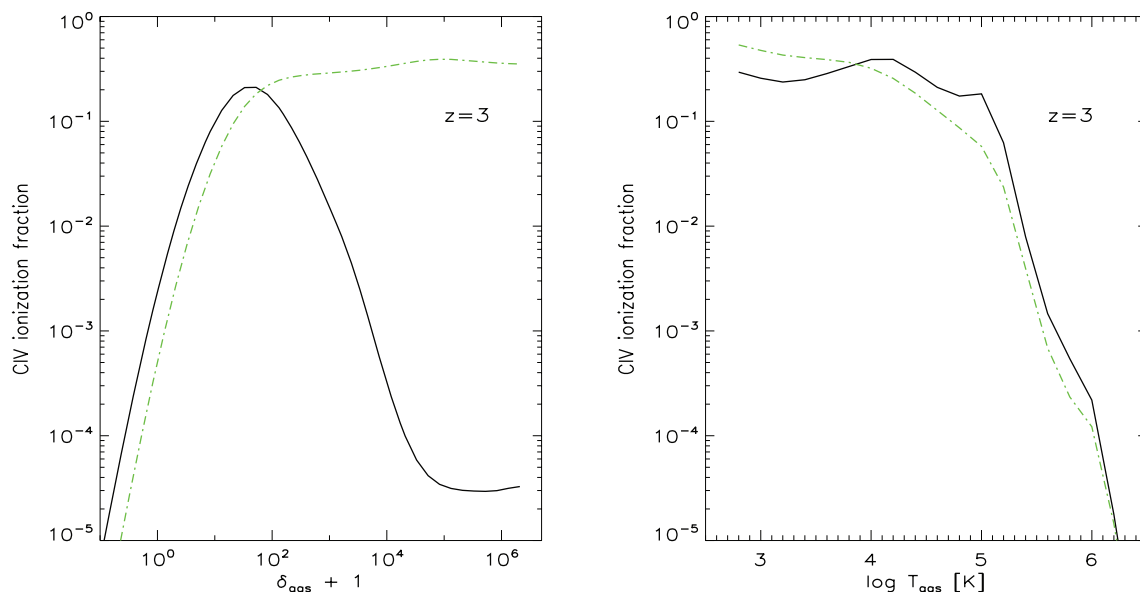
Figure 1. Left-hand panel: C IV ionization fraction, as a function of the gas overdensity, at $z = 3$ for a gas temperature of $10^{4.6}$ K (solid black line) and $10^{5.0}$ K (dot–dashed green line). Right-hand panel: C IV ionization fraction, as a function of the gas temperature, at $z = 3$ for an overdensity of $\delta_{gas} \sim 50$ (solid black line) and $\delta_{gas} \sim 10$ (dot–dashed green line).

to 2×400^3. This simulation is identical to kr37edw500, except for the larger number of particles and was run in order to check for resolution effects.

The name of each simulation reflects the choice of the IMF, the box size (even if the box size is equal to 37.5 h^{-1} Mpc for all the simulations, we report it in order to be consistent with other works, e.g. Oppenheimer & Davé 2006, 2008) and the feedback prescription adopted (only in the case of the resolution-test run, kr37p400edw500, the number of particles is specified in the name). In this paper, we label as 'reference runs' the first three of the list above: kr37edw500, kr37mdw and kr37agn.

We use the CLOUDY code (Ferland et al. 1998) to compute a posteriori the C IV ionization fractions for each gas particle. As for the work presented in Tescari et al. (2009), we choose the HM05 option in CLOUDY, which consists of a UVB made by QSOs and galaxies with a 10 per cent photon escape fraction and which is in agreement with other observational constraints (Bolton et al. 2005). In the left-hand panel of Fig. 1, we plot the C IV ionization fraction as a function of the gas overdensity $\delta_{gas} + 1 = \rho_{gas}/\bar{\rho}$, at $z = 3$ for a gas temperature of $10^{4.6}$ K (solid black line) and $10^{5.0}$ K (dot–dashed green line). In the right-hand panel, we plot the same ionization fraction, as a function of the gas temperature T_{gas}, at $z = 3$ for an overdensity of $\delta_{gas} \sim 50$ (solid black line), this value being representative of the outskirts of dark matter haloes and $\delta_{gas} \sim 10$ (dot–dashed green line).

4 STAR FORMATION RATES AND EVOLUTION OF THE TOTAL CARBON CONTENT

In this Section, we analyse the cosmic SFRs and the evolution of the total carbon content in the different simulations.

In the left-hand panel of Fig. 2, we report the total SFR of the simulated volume as a function of redshift. All the simulations, except the kr37p400edw500 run, have the same SFR down to redshift $z \sim 9.5$, when they start to differ due to their distinct feedback recipes. Run kr37nf (no-feedback, green dots) has the highest SFR

compared to the other runs because there is no effective mechanism that is able to quench the star formation. Run kr37agn (AGN feedback, black dots) follows the no-feedback run kr37nf down to redshift $z = 3$, but then the AGN feedback becomes effective and the SFR suddenly decreases. Runs kr37co-edw500 (coupled EDW, red dots), kr37edw500 (EDW, cyan dots) and kr37mdw (MDW, blue dots) show more or less the same trend, but for the kr37co-edw500 the SFR is slightly higher due to the fact that the coupled winds are less efficient than the normal winds in making the central region of the haloes devoid of gas and therefore in suppressing the star formation. The kr37agn+edw300 simulation (AGN + EDW, yellow dots) follows the other 'wind' runs (kr37co-edw500, kr37edw500 and kr37mdw) until redshift $z = 3$, but then the AGN feedback starts to become active and suppresses the star formation very efficiently. Finally, at $z > 8$, the kr37p400edw500 run (resolution test, grey dots) shows a higher star formation with respect to the other runs due to the improved resolution of this simulation that can resolve higher densities at earlier times. Going to lower redshift, the SFR of kr37p400edw500 agrees very well with that of the kr37edw500 run, which has the same box size and parameters but poorer resolution. This confirms the numerical convergence of our simulations in the regime we are interested in. We stress that the aim of this plot is to underline the effect of the different feedback prescriptions on the SFR. For this reason observational data are not plotted, because our simulations can be tuned in order to fit the observed cosmic SFR at low redshift and, in this sense, kr37edw500 is the reference simulation: all the other runs in this plot differ only for the feedback prescription (all of them have Kroupa IMF) and were not retuned. We also did not plot the two runs with different IMFs, ay37edw500 (Arimoto–Yoshii IMF) and sa37edw500 (Salpeter IMF), because we do not change the star formation efficiency as it would be required in order to match the observables when the number of massive stars per unit mass of formed stars changes: we are more interested in the chemical and energetic effect of the IMF.

In the right-hand panel of Fig. 2, we show the evolution with redshift of the carbon cosmological mass density $\Omega_C(z)$, calculated
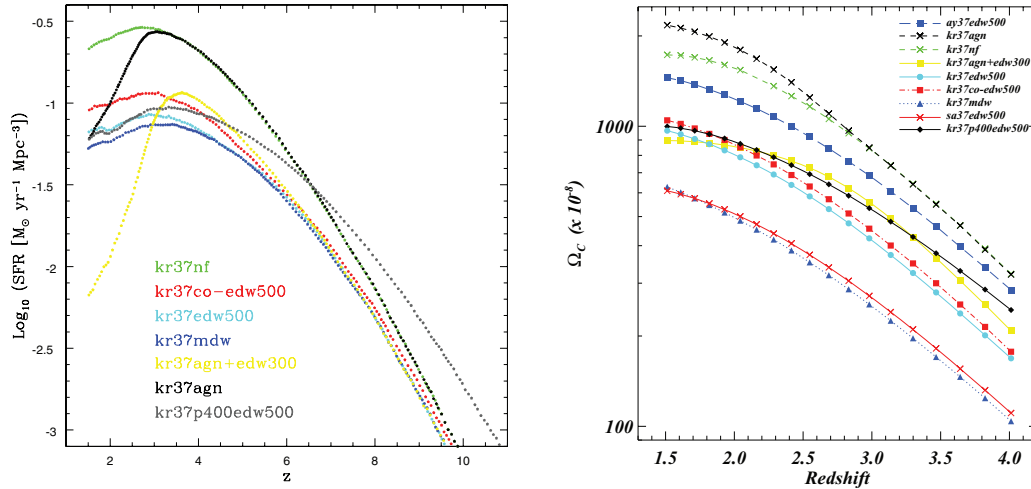
Figure 2. Left-hand panel: cosmic SFR for some of the hydrodynamic simulations of Table 2. Right-hand panel: evolution of the total Ω_C as a function of redshift for all the hydrodynamic simulations of Table 2.

considering the sum of the carbon content associated to each particle inside the cosmological box. EDW runs kr37edw500 (cyan circles–triple-dot–dashed line), ay37edw500 (blue squares–dashed line) and sa37edw500 (red crosses–solid line) are identical except for the IMF; therefore the comparison of these three simulations is useful to understand how carbon production is affected by the choice of the IMF. The evolution of Ω_C is in fact the same, but with different normalization: ay37edw500 has Arimoto–Yoshii IMF and produces more carbon than the kr37edw500 run (Kroupa IMF), which itself produces more carbon than sa37edw500 (Salpeter IMF). With the Kroupa IMF, the relative fraction of intermediate-mass stars, i.e. stars with masses $2\,\mathrm{M_\odot} \leq m \leq 8\,\mathrm{M_\odot}$, representing important carbon producers, is larger than with the Salpeter IMF (Calura & Matteucci 2006; Calura & Menci 2009). For this reason, Ω_C obtained with the Kroupa IMF is higher than that obtained with the Salpeter IMF. On the other hand, the assumption of a top-heavy IMF, such as the one of Arimoto & Yoshii (1987), strongly enhances the number of massive stars but suppresses the fraction of intermediate-mass stars, with the overall result of a higher carbon density at any cosmic epoch. Interestingly, run kr37mdw (MDW, blue triangles–dotted line) follows sa37edw500 even if the latter produces much less C IV as we will show in Section 7 (Fig. 12, left-hand panel). Run kr37co-edw500 (coupled EDW, red squares–dot–dashed line) has the same trend as kr37edw500, but with a slightly higher normalization. As we stated above, this is due to the fact that the coupled winds are less efficient than the normal winds and therefore this simulation has a higher star formation that results in a higher carbon abundance. This situation is even more extreme for the kr37nf (no-feedback, green crosses–dashed line) and kr37agn (AGN feedback, black crosses–dashed line) runs; in fact down to redshift $z \sim 3$ both of these simulations do not suppress effectively the star formation, and for them Ω_C is higher. Going to lower redshift, AGN feedback becomes active in quenching the star formation and lowers the amount of gas used by the stars and converts in other species (note the excess in Ω_C with respect to the kr37nf run at $z < 2.7$). The kr37agn+edw300 run (AGN + EDW, yellow squares–solid line) shows the same Ω_C trend of kr37edw500 even with higher normalization at high redshift due to the lower strength of the winds ($300\,\mathrm{km\,s^{-1}}$ instead of $500\,\mathrm{km\,s^{-1}}$). At low redshift, AGN feedback becomes active but differently from the kr37agn case: (i) winds have already made the haloes devoid of gas,

therefore reducing the efficiency of the BH accretion and thus the power of the AGN feedback; (ii) winds suppress star formation at high redshift lowering the carbon content, so when the AGN starts to work the net result is a further decrease of Ω_C. Finally, at high redshift the kr37p400edw500 run (resolution test, black diamonds–solid line) shows a higher Ω_C with respect to kr37edw500 due to the improved resolution of this simulation (as explained above), while at low redshift the carbon content of kr37p400edw500 approaches that of the kr37edw500 run.

Comparing the Ω_C evolution of our simulations with the one showed in Oppenheimer & Davé (2006; Fig. 12), we found that in general the normalization of our runs is higher, although a very precise comparison is not possible given the different set-up of the simulations used, especially regarding the chemical evolution model. However, for the kr37mdw run (and also for the sa37edw500 run) the agreement is much better, the latter simulation producing momentum-driven galactic winds and therefore being the yardstick for the comparison with the Oppenheimer & Davé (2006) work.

5 STATISTICS OF H I

Before focusing on the C IV evolution, we address some flux statistics related to the properties and the evolution of neutral hydrogen in the IGM. For all the neutral hydrogen statistics discussed in this paper, we considered H I *lines* (while for the C IV we considered from time to time lines or systems of lines).

For each simulation performed, we have extracted several physical quantities interpolated along lines of sight (LOSs) through the box. Given the positions, velocities, densities and temperatures of all SPH particles at a given redshift, we compute spectra along a given LOS through the box following the procedure of Theuns et al. (1998). We divide the sight-line into $N = 1024$ bins of width Δ in distance x along the sight-line. For a bin i at position $x(i)$, we compute the density and the density weighted temperature and velocity from

$$\rho_X(j) = a^3 \sum_i X(i)\mathcal{W}_{ij}, \tag{7}$$

$$(\rho T)_X(j) = a^3 \sum_i X(i)T(i)\mathcal{W}_{ij}, \tag{8}$$

$$(\rho v)_X (j) = a^3 \sum_i X(i)\{a\dot{x}(i) + \dot{a}[x(i) - x(j)]\}\mathcal{W}_{ij}, \qquad (9)$$

where a is the scalefactor, $X(i)$ is the abundance of species X of SPH particle i, assuming ionization equilibrium, and $\mathcal{W}_{ij} = m W(q_{ij})/h_{ij}^3$ is the normalized SPH kernel. Here W is the SPH kernel, m is the SPH particle mass and

$$q_{ij} = \frac{a\,|x(i) - x(j)|}{h_{ij}}, \qquad (10)$$

$$h_{ij} = \frac{1}{2}\left[h(i) + h(j)\right], \qquad (11)$$

with h the physical softening scale. The optical depths of the simulated QSO spectra are drawn in redshift space taking into account the effect of the IGM peculiar velocities along the LOS, $v_{\mathrm{pec},\parallel}$.

Taking the case of H I, even if the neutral hydrogen fraction $f_{\mathrm{H I}}$ is associated to each gas particle and is stored in each simulation snapshot, we follow Nagamine, Springel & Hernquist (2004), as in Tescari et al. (2009), to assign a posteriori a new mass in neutral hydrogen to gas particles above the density threshold for the onset of the star formation (set to $\rho_{\mathrm{th}} = 0.1$ cm^{-3} in terms of the number density of hydrogen atoms) which reads

$$m_{\mathrm{H I}} = f_{\mathrm{H I}} m_{\mathrm{H}} \quad (\rho < \rho_{\mathrm{th}}), \qquad (12)$$

$$m_{\mathrm{H I}} = f_{\mathrm{c}} m_{\mathrm{H}} \quad (\rho \geq \rho_{\mathrm{th}}), \qquad (13)$$

with $f_{\mathrm{H I}}$ the neutral hydrogen fraction that depends on the UVB used, m_{H} the hydrogen mass of the particle ($f_{\mathrm{H I}}$ and m_{H} are determined self-consistently inside the code), f_{c} the fraction of mass in cold clouds and ρ_{th} the star formation threshold. Here $f_{\mathrm{c}} = \rho_{\mathrm{c}}/\rho$, where ρ_{c} is the density of cold clouds and ρ the total (hot + cold) gas density. Individual molecular clouds cannot be resolved at the resolution reachable in cosmological simulations, thus ρ_{c} represents an average value computed over small regions of the ISM (Springel & Hernquist 2003).

Our code follows self-consistently the evolution of carbon (and of other elements; see Section 3), then, using the CLOUDY code (Ferland et al. 1998), we determine the ionization fractions for C IV ($\lambda\lambda$ 1548.204, 1550.781 Å). The simulated flux of a given ion transition at the redshift-space coordinate u (in km s^{-1}) is $F(u) = \exp[-\tau(u)]$ with

$$\tau(u) = \frac{\sigma_{0,\mathrm{I}}\,c}{H(z)} \int_{-\infty}^{\infty} n_{\mathrm{I}}(x)\,\mathcal{V}\left[u - x - v_{\mathrm{pec},\parallel}^{\mathrm{IGM}}(x),\,b(x)\right]\,\mathrm{d}x, \qquad (14)$$

where n_{I} is the ion number density, $\sigma_{0,\mathrm{I}}$ is the cross-section of the particular ion transition, $H(z)$ is the Hubble constant at redshift z, x is the real-space coordinate (in km s^{-1}), $b = (2k_{\mathrm{B}}T/m_{\mathrm{I}}c^2)^{1/2}$ is the velocity dispersion in units of c and $\mathcal{V}$ is the Voigt profile. These spectra can be converted from velocity v to observed wavelength λ using $\lambda = \lambda_0(1 + z)(1 + v/c)$.

After having extracted the spectra along random LOS through the cosmological box for a given simulation at a given redshift z, we rescaled all the H I optical depths by a constant factor $A_{\mathrm{H I}}$ (ranging from $\sim$0.43 to $\sim$0.73, depending on redshift) in such a way that their mean value was equal to the H I effective optical depth, $\tau_{\mathrm{H I}}^{\mathrm{eff}}$, at that redshift given by the Kim et al. (2007) fitting formula:

$$\tau_{\mathrm{H I}}^{\mathrm{eff}} = (0.0023 \pm 0.0007)(1 + z)^{3.65 \pm 0.21}. \qquad (15)$$

This rescaling ensures that our spectra match the observed mean normalized flux of the Lyman α forest at the appropriate redshift: $\langle F \rangle_{\mathrm{H I,obs}} = \exp\left(-\tau_{\mathrm{H I}}^{\mathrm{eff}}\right)$. We also rescaled all the C IV optical depths for the same constant factor $A_{\mathrm{H I}}$. Then we convolved the spectra with

a Gaussian of 6.6 km s^{-1} full width at half-maximum (FWHM) and we added noise in order to have realistic spectra, with S/N = 50, to compare with observations. Finally, we run the VPFIT code to fit each spectra and recover H I and C IV lines' redshift, column density and Doppler parameter. Among the lines fitted by VPFIT, we have considered only those with relative errors in the Doppler parameter lower than 50 per cent.

5.1 The H I column density distribution function

In this Section, we compute the Lyman α forest CDDF (H I CDDF) $\mathrm{d}^2 n/\mathrm{d}N\,\mathrm{d}z$, namely the number of absorbers with H I column density in the range $[N, N + \mathrm{d}N]$ and redshift path in the interval $[z, z + \mathrm{d}z]$. The redshift path at a given redshift z in simulated spectra is given by

$$\mathrm{d}z = n_{\mathrm{spec}}(1 + z)\frac{\Delta v}{c}, \qquad (16)$$

where c is the speed of light (in km s^{-1}) and n_{spec} is the number of spectra taken at z for a simulation with box size in km s^{-1} equal to Δv.

In Fig. 3 we show the H I CDDF at redshift $z = 3$ for all the simulations of Table 2 splitted in two groups for the sake of clarity. All the simulations fit very well the observational data by D'Odorico et al. (2008) down to column density $\log N_{\mathrm{H I}}\,(\mathrm{cm}^{-2}) = 12.2$ and are all in agreement confirming the fact that the H I CDDF is quite insensitive to the different feedback prescriptions. Even though the galaxies drive strong winds or AGN feedbacks, there is no discernible effect on the Lyman α forest. This is due to the fact that winds or BH ejecta expand preferentially into the lower density regions and so keep the filaments that produce the hydrogen lines intact (Theuns et al. 2002). The volume filling factor of the winds is thus quite small and does not impact strongly on Lyman α lines. In Fig. 4 we show the H I CDDF at redshift $z = 2.25$: all the previous trends are confirmed and the agreement to the data is very good also for $\log N_{\mathrm{H I}}\,(\mathrm{cm}^{-2}) < 12$.

5.2 Probability distribution function of the H I Doppler parameter

In this Section we analyse the Lyman α Doppler parameter, $b_{\mathrm{H I}}$, probability distribution function. Throughout the rest of the paper, both the H I and the C IV Doppler parameters are assumed to be due only to the thermal width of the line and we neglect possible turbulent contribution. Therefore, omitting the turbulent contribution, the Doppler parameter basically measures the temperature of the gas and is defined as

$$b_{\mathrm{H I}} = \sqrt{\frac{2k_{\mathrm{B}}T}{m_{\mathrm{H I}}}}, \qquad (17)$$

where $m_{\mathrm{H I}}$ is the neutral hydrogen particle mass and k_{B} is the Boltzmann's constant. In Figs 5 and 6, we show the Lyman α Doppler parameter distribution function at redshift $z = 3$ and 2.25, respectively, for all the simulations of Table 2, splitted in two groups and compared with the data by D'Odorico et al. (2008; purple solid line, while the shaded region represents the 1σ Poissonian error). All runs are in good agreement with each other while they are shifted towards higher $b_{\mathrm{H I}}$ values with respect to the observational data. At redshift $z = 3$, the median value of the observational Doppler parameters distribution is 25.9 km s^{-1}, while all the simulations have median around $\sim$34.5 km s^{-1}. At $z = 2.25$, the data by D'Odorico
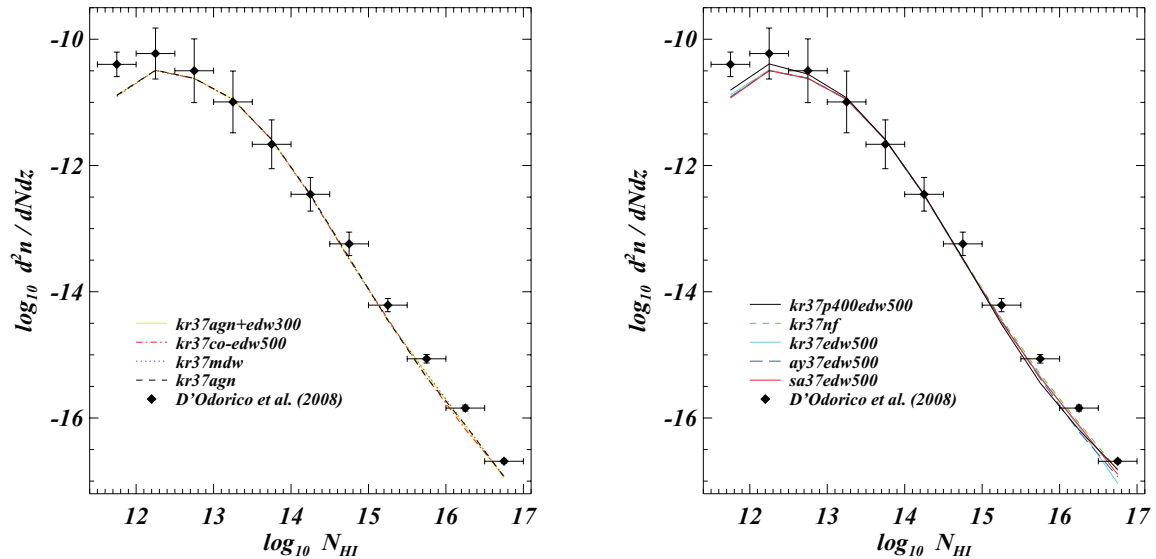
Figure 3. Neutral Hydrogen (H I) CDDF at $z = 3$. Left-hand panel: part I (first set of simulations). Right-hand panel: part II (second set of simulations). Data from D'Odorico et al. (2008).
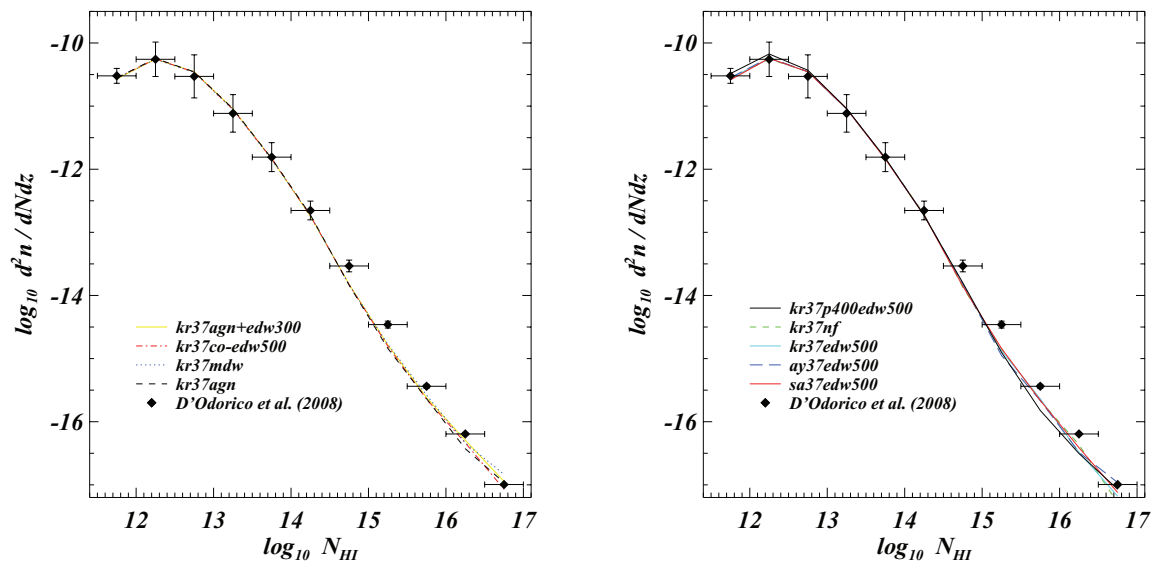

Figure 4. As in Fig. 3, but at redshift $z = 2.25$.

et al. (2008) have median value equal to $24.8 \, \text{km s}^{-1}$, while the simulations have median around $\sim 34.9 \, \text{km s}^{-1}$.

Our simulations produce H I gas that is too hot compared to the observations. There can be many reasons for this, both physical and numerical. Regarding the former, it is very important to stress the effect of the UV background on the gas: if the UV background is too strong the gas will be heated too much. As stated in Section 3, we multiplied the Haardt & Madau (1996) heating rates by a factor of 3.3, introduced to fit the Schaye et al. (2000b) constraints on the temperature evolution of the IGM. It seems that this correction does not work properly with new and higher quality data sets.

However, minor part of the discrepancy is due to the lines-fitting procedure. When the absorption lines are weak and not well defined, VPFIT can add relatively broad components in order to minimize the χ^2 statistics. This spurious components could have large equivalent

width and low optical depth; therefore they have negligible impact on the CDDF because of their relative small column density, but they can bias the Doppler parameter probability distribution function. We will show later in Section 9 that this numerical effect is more evident for the C IV statistics and how it is important in explaining some features of the $b_{C\,IV}$–$N_{C\,IV}$ relation.

5.3 Column density–Doppler parameter relation

In Figs 7 and 8, we plot the $b_{H\,I}$–$N_{H\,I}$ relation at redshift $z = 3$ and 2.25, respectively, for the reference simulations kr37edw500, kr37mdw and kr37agn. The contour plots are colour coded according to the fraction of points that fall in each bin with coordinate $(b_{H\,I}, N_{H\,I})$. In the upper left-hand panels, the observational data of D'Odorico et al. (2008) are reported. Both at redshift $z = 3$ and 2.25

Figure 5. Linewidths b_{HI} probability distribution function at $z = 3$. Left-hand panel: part I. Right-hand panel: part II. In both panels, data from D'Odorico et al. (2008) are showed by the purple solid line along with the associated Poissonian error (shaded region).
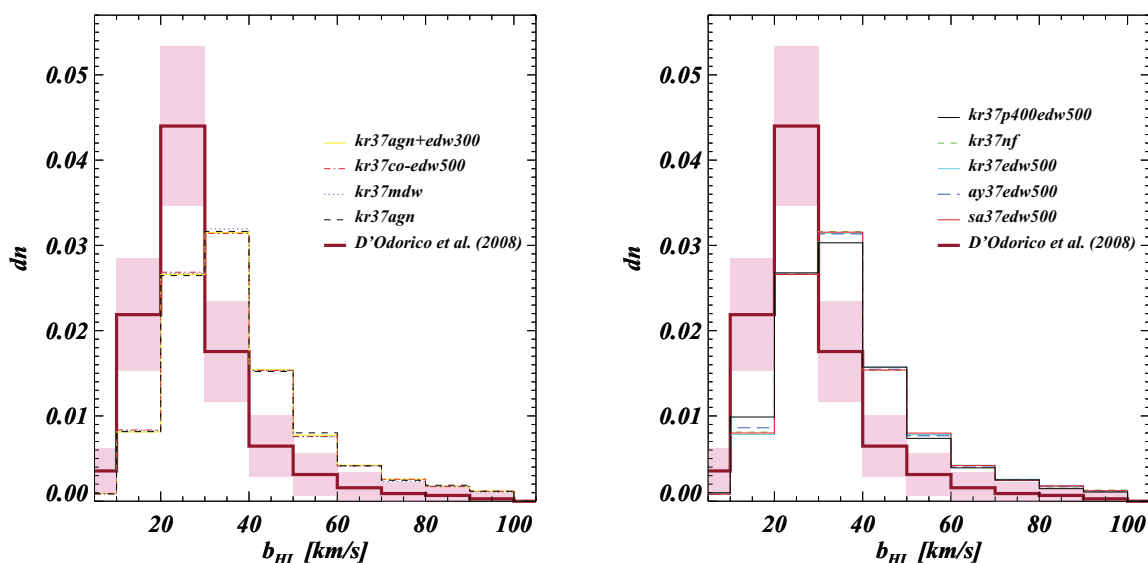

Figure 6. As in Fig. 5, but at redshift $z = 2.25$.

all runs are in good agreement with each other and reproduce well the observations, even if the simulations present Doppler parameters slightly higher than the observational data (as we mentioned in the previous Section). The mean slope of the data envelope in the column density range $11.5 < \log N_{HI}\,(\mathrm{cm}^{-2}) < 15$ measures the slope of the T–ρ relation for the gas (Schaye 2001), and all the runs show roughly the same right slope of the data at the two redshift.

To sum up, the fact that for our simulations all the different H I statistics are in general agreement with the observational data confirms that we are catching the physics of the gas traced by the neutral hydrogen. The discrepancies are due, mainly, to the choice of the UV background [assumed to be produced by quasars and galaxies as given by Haardt & Madau (1996), with the heating rates multiplied by a factor of 3.3; see Sections 3 and 5.2] and, in minor part, to a numerical effect introduced by VPFIT that affects our

analysis of the absorption lines in quasar spectra. We will discuss in more detail the impact of this effect in the next sessions regarding the C IV absorption lines statistics.

The resolution-test simulation kr37p400edw500 follows the other runs in all the previous statistics, again confirming the numerical convergence of our simulations for the H I evolution.

6 THE C IV COLUMN DENSITY DISTRIBUTION FUNCTION

In this Section we investigate the C IV CDDF (C IV CDDF; already defined in Section 5.1), plotted at redshift $z = 3$, 2.25 and 1.5, respectively and along with the D'Odorico et al. (2010) data, in Figs 9, 10 and 11. We considered for this analysis *systems* of lines as defined in Section 2.
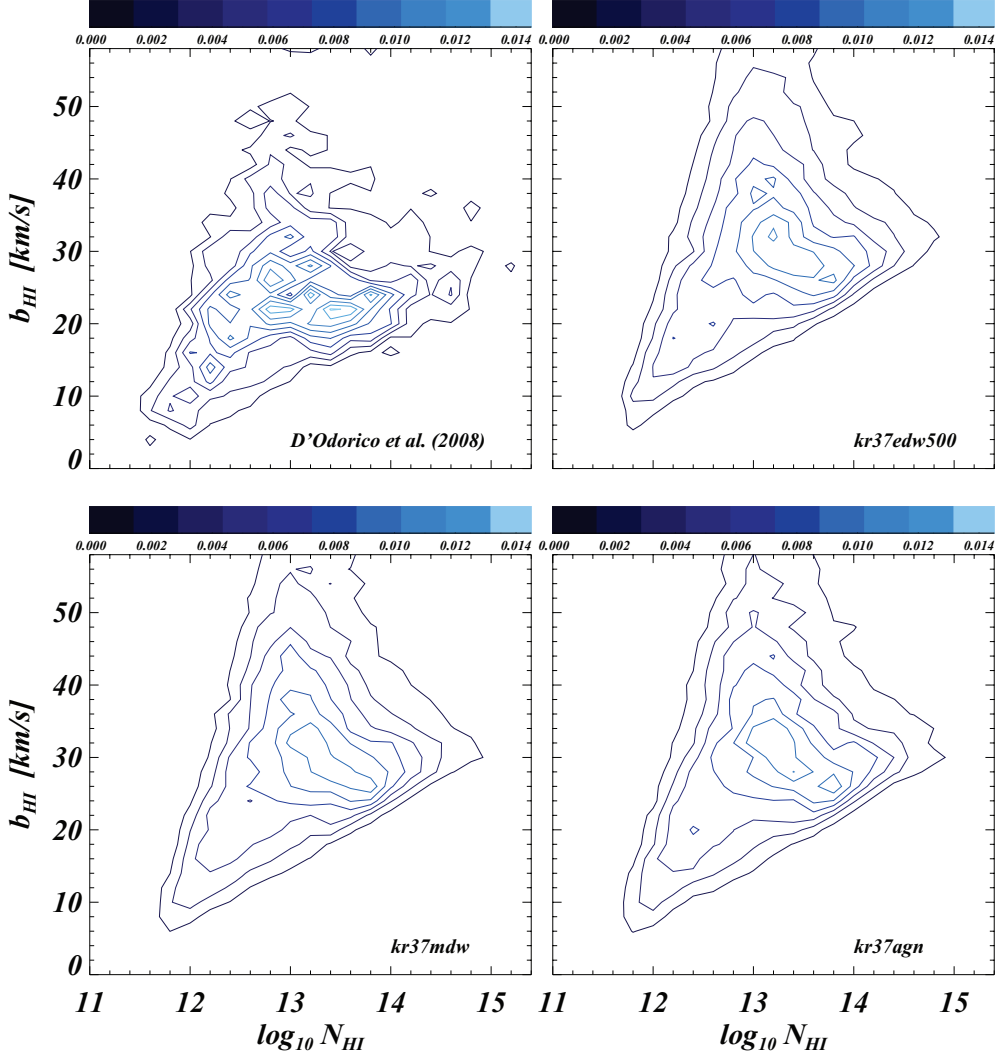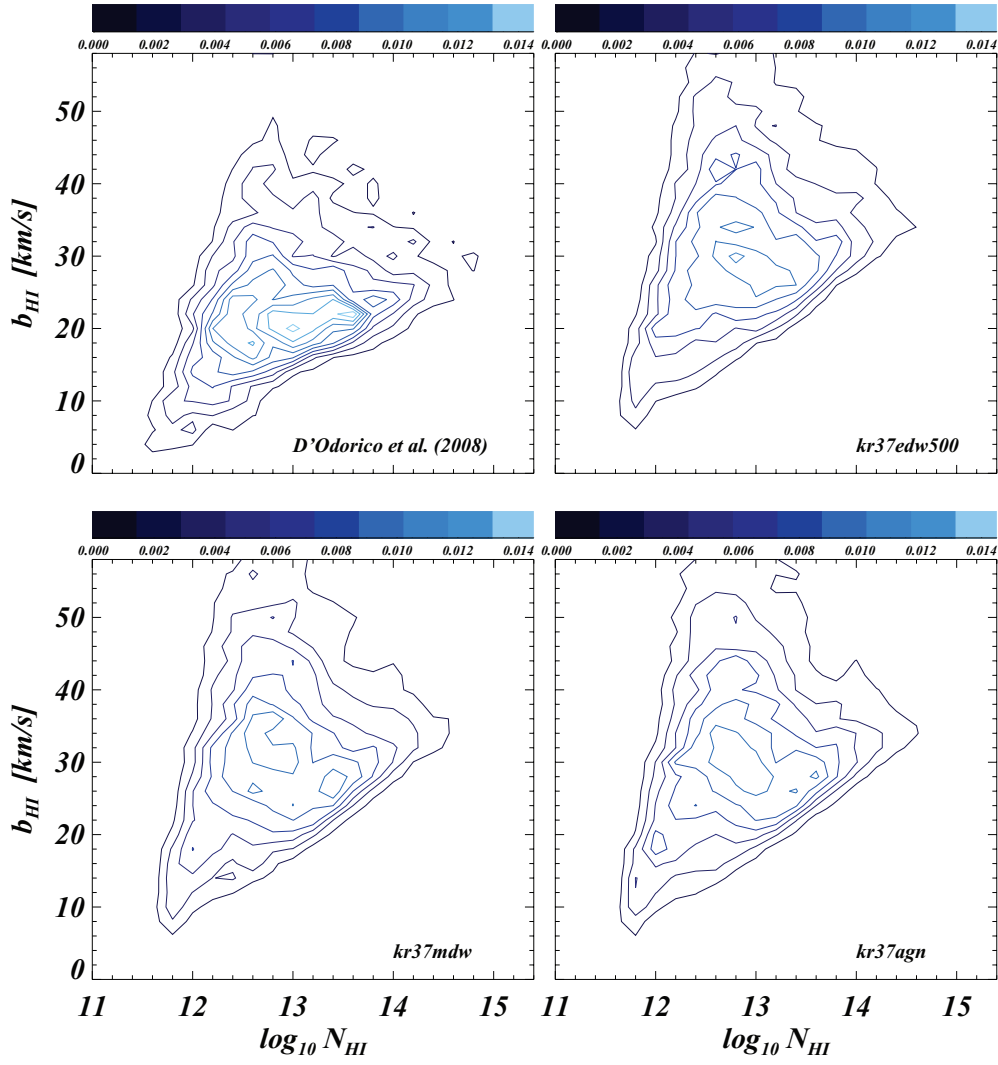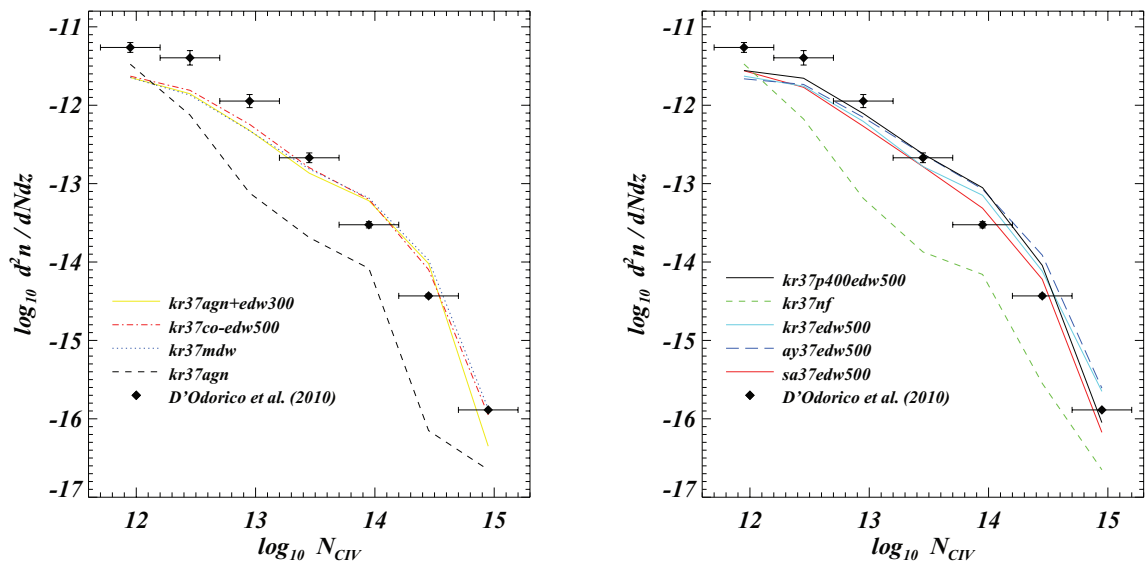
Figure 7. b_{H_I}–N_{H_I} relation at $z = 3$. The horizontal bars are colour coded according to the fraction of points that fall in each bin with coordinate (b_{H_I}, N_{H_I}). Upper left-hand panel: observational data from D'Odorico et al. (2008).

At $z = 3$ (Fig. 9), runs (left-hand panel) kr37agn+edw300 (AGN + EDW), kr37co-edw500 (coupled EDW) and kr37mdw (MDW) and (right-hand panel) kr37edw500 (EDW, Kroupa IMF), ay37edw500 (EDW, Arimoto–Yoshii IMF) and sa37edw500 (EDW, Salpeter IMF) are in agreement with each other and reproduce well the observed distribution down to $\log N_{C_{IV}}(\text{cm}^{-2}) \sim 12.7$. In contrast, for the simulations kr37nf and kr37agn the agreement is not good. Simulation kr37nf (Fig. 9 right-hand panel, green dashed line) was run, as a test, without any winds or AGN feedback: so there is no effective mechanism to spread the enriched gas outside the haloes. The result is that all the gas is trapped inside high-density haloes and most of the carbon is locked back into stars. In run kr37agn (Fig. 9 left-hand panel, black dashed line) the feedback mechanism is the AGN feedback, associated to the energy released by gas accretion on to supermassive BHs. Comparing the resulting distribution with that of kr37nf, we note that they are very similar. The reason is that at redshift $z = 3$ the AGN feedback is not active yet, but it is just starting to work, so at high redshift this simulation virtually behaves like the no-feedback one. Interestingly, run kr37agn+edw300 (AGN + EDW) follows all the other 'wind' runs even if in this case we have the combined effect of wind and AGN

feedbacks: this is due to the fact that winds start to be effective at higher redshift than the AGN feedback, making the haloes devoid of gas and in this way reducing the efficiency of the BH accretion and the power of the AGN feedback.

At redshift $z = 2.25$ (Fig. 10), the agreement with observational data is very good down to $\log N_{C_{IV}}$ (cm^{-2}) = 12. The kr37nf run (no-feedback; right-hand panel, dashed green line) suffers from the same problems described before, while for the kr37agn run (AGN feedback; left-hand panel, dashed black line) the discrepancies with the observational data decreased: a first hint that going to lower redshift, AGN feedback becomes more and more efficient and the behaviour of this simulation starts to resemble that of the 'wind' runs.

At redshift $z = 1.5$ (Fig. 11), all the simulations produce too many systems with low column density and systematically fall slightly short of reproducing the distribution at $\log N_{C_{IV}}$ (cm^{-2}) > 14.5. Now the kr37agn run (AGN feedback; left-hand panel, dashed black line) closely follows all the other runs, confirming that at this low redshift AGN feedback is active and powerful, while kr37nf run (no-feedback; right-hand panel, dashed green line) still fails in reproducing the correct trend. For this statistics, at the three redshift

Figure 8. As in Fig. 7, but at redshift $z = 2.25$.

Figure 9. C IV CDDF at $z = 3$. Left-hand panel: part I. Right-hand panel: part II. Data from D'Odorico et al. (2010).
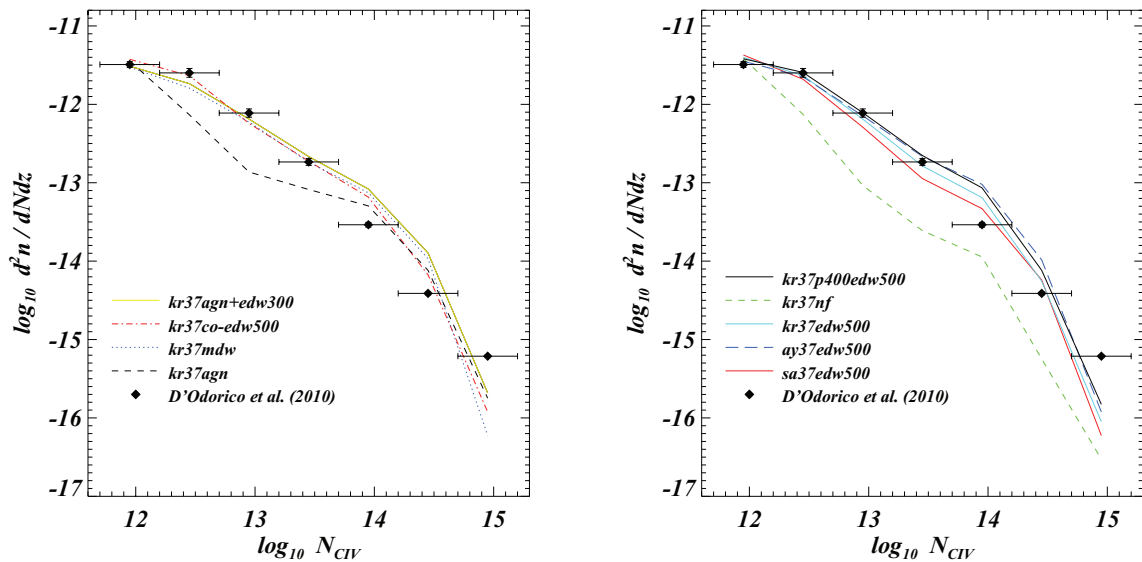
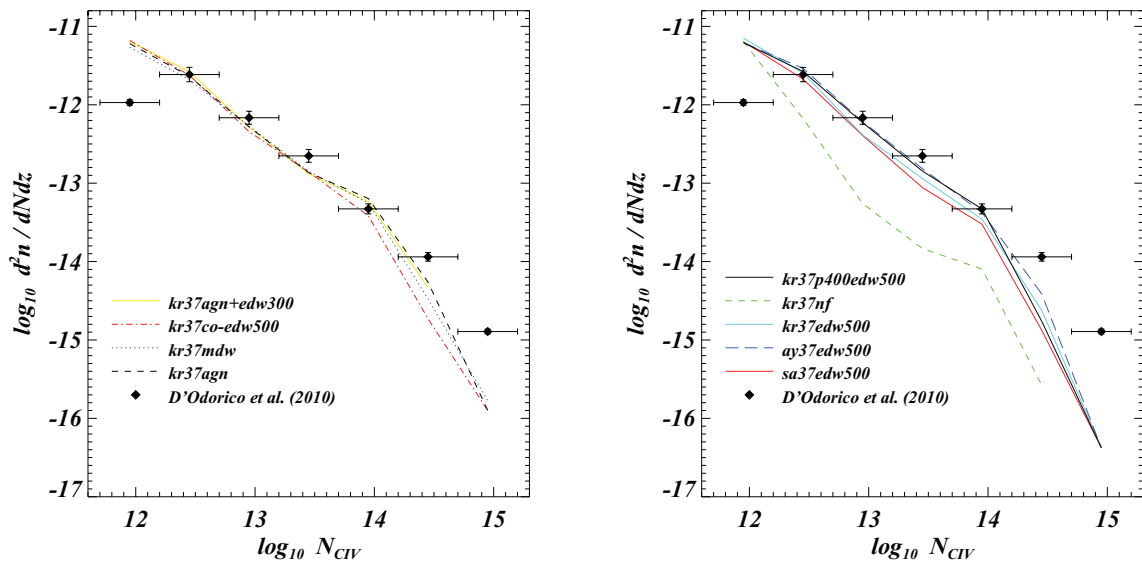**Figure 10.** As in Fig. 9, but at redshift $z = 2.25$.

Figure 11. As in Fig. 9, but at redshift $z = 1.5$.

considered, the resolution-test simulation kr37p400edw500 follows the reference runs.

Note that at redshift $z = 2.25$ we fit very well the observational data in the low column density tail of the distribution, $\log N_{C\,IV}$ (cm^{-2}) < 12.2, while at $z = 3$ and 1.5 the agreement in this column density range gets worse.

7 THE EVOLUTION OF THE C IV COSMOLOGICAL MASS DENSITY

In the left-hand panel of Fig. 12 we show $\Omega_{C\,IV}(z)$, calculated considering the sum of the C IV content associated to each particle inside the cosmological box. EDW runs kr37edw500 (cyan circles–triple-dot–dashed line), ay37edw500 (blue squares–dashed line) and sa37edw500 (red crosses–solid line) behave exactly as we described in Section 4: they differ only for the IMF and ay37edw500

produces much more C IV than the other two, having Arimoto–Yoshii IMF. Runs kr37co-edw500 (coupled EDW; red squares–dot–dashed line) and kr37mdw (MDW; blue triangles–dotted line) follow almost the same trend as kr37edw500, which has the same IMF as that of the two runs mentioned above. For the kr37nf simulation (no-feedback; green crosses–dashed line), $\Omega_{C\,IV}$ starts to decrease at redshift $z \sim 2.7$. It is interesting to note that for the simulation kr37agn (AGN feedback; black crosses–dashed line), $\Omega_{C\,IV}$ suddenly increases after a small decrement at redshift $z \sim 2.8$ (down to this redshift the kr37agn run follows the no-feedback run). This is due to the suppression of star formation produced by the powerful AGN feedback. Then, moving to lower redshift the C IV cosmological density starts to approach all the other runs. The same effect is visible in the kr37agn+edw300 run (AGN + EDW; yellow squares–solid line). In this case the effect is weaker because, as we explained in Section 6, winds make haloes devoid of gas,
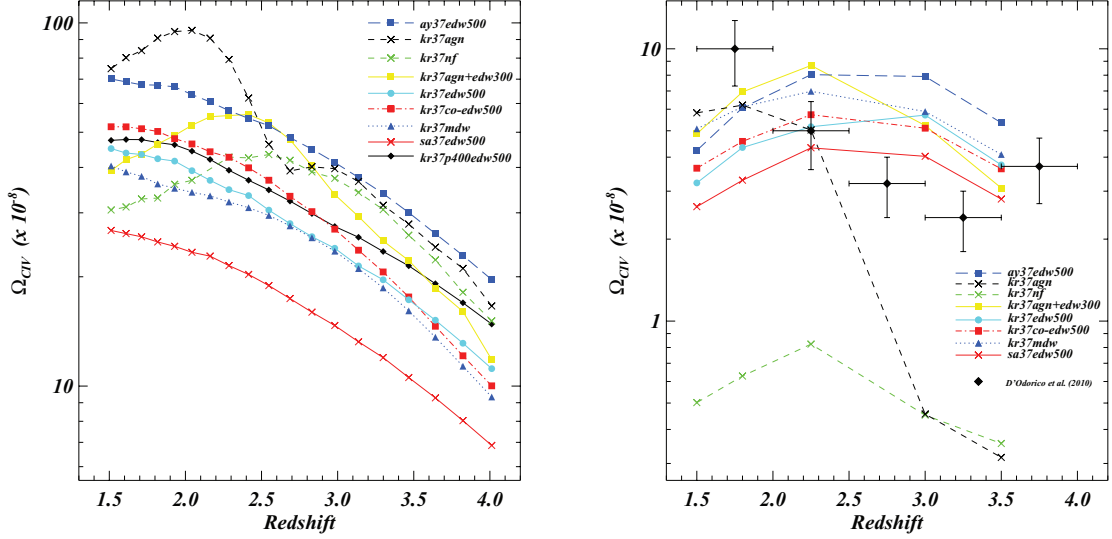
Figure 12. Left-hand panel: evolution of the total $\Omega_{\text{C IV}}$ as a function of redshift for all the hydrodynamic simulations of Table 2. Right-hand panel: $\Omega_{\text{C IV}}$ evolution with redshift, calculated considering the absorption lines in 1000 LOSs through each box, for the different simulation boxes. The overplotted black diamonds show the observational data of D'Odorico et al. (2010).

therefore reducing the efficiency of the BH accretion and thus the power of the AGN feedback. As for the total Ω_C plot in the right-hand panel of Fig. 2, at high redshift, the resolution-test simulation kr37p400edw500 shows a higher $\Omega_{\text{C IV}}$ with respect to the kr37edw500, while the two runs are in agreement at low redshift.

In the right-hand panel of Fig. 12, we show the evolution with redshift of the C IV cosmological mass density as a fraction of the critical density today, calculated considering the CDDF of the C IV absorption lines:

$$\Omega_{\text{C IV}}(z) = \frac{H_0 m_{\text{C IV}}}{c \rho_{\text{crit}}} \int N f(N) \, \mathrm{d}N, \qquad (18)$$

where $H_0 = 100 \, h \, \text{km s}^{-1} \, \text{Mpc}^{-1}$ is the Hubble constant ($h = 0.73$), $m_{\text{C IV}}$ is the mass of a C IV ion, c is the speed of light, $\rho_{\text{crit}} = 1.88 \times 10^{-29} \, h^2 \, \text{g cm}^{-3}$ and $f(N)$ is the C IV CDDF. Since $f(N)$ cannot be recovered correctly for all the column densities due to incompleteness and poor statistics, the integral in the previous equation can be approximated by a sum (Storrie-Lombardi, McMahon & Irwin 1996):

$$\Omega_{\text{C IV}}(z) = \frac{H_0 m_{\text{C IV}}}{c \rho_{\text{crit}}} \frac{\sum_i N_i(\text{C IV})}{\Delta X}, \qquad (19)$$

with $\Delta X \equiv \int (1+z)^2 [\Omega_{0m}(1+z)^3 + \Omega_{0\Lambda}]^{-1/2} \, \mathrm{d}z$, the redshift absorption path. In the right-hand panel of Fig. 12, the overplotted black diamonds show the observational data of D'Odorico et al. (2010). The value of $\Omega_{\text{C IV}}$ significantly depends on the column density range over which the sum or the integration is carried out and, as a consequence, on the resolution and S/N of the available spectra. In order to address this aspect, D'Odorico et al. (2010) have computed three sets of values to be compared consistently with different data in the literature. Here we compared $\Omega_{\text{C IV}}$ obtained from the simulated C IV *systems* (as defined in Section 2) lying in the column density range $12 \leq \log N_{\text{C IV}} \, (\text{cm}^{-2}) \leq 15$, with the $\Omega_{\text{C IV}}$ computed from the C IV systems of the total D'Odorico et al. (2010) sample, in the same range of column densities. From $z = 3.5$ to 2.5 all the simulations, except for the kr37nf (no-feedback) and the kr37agn (AGN feedback), roughly reproduce the observational data and show an increasing or constant trend for the $\Omega_{\text{C IV}}$. Down

to redshift $z = 3$, the AGN feedback of run kr37agn is not active and the C IV content is nearly equal to the one of the no-feedback simulation kr37nf. At $z = 3$, the AGN feedback starts to work and the kr37agn run suddenly reaches all the other 'wind' simulations.

Apart from the no-feedback simulation kr37nf (green crosses and dashed line), all the other runs still reproduce the observational data around redshift $z = 2.25 \pm 0.25$. If we consider lower redshift, all the simulations show a decreasing trend at variance with the data. Different is the case of the kr37agn run: from redshift $z = 3.0$ to 1.8, the AGN feedback suppresses efficiently the star formation, therefore the gas is no longer reprocessed from the stars and the C IV is not converted in other ions. At the same time, the AGN feedback has not yet made the haloes devoid of gas, with the result that $\Omega_{\text{C IV}}$ continues to increase. However, since the BH accretion feedback is extremely powerful, moving to lower redshift a considerable amount of gas is expelled from the haloes and heated. As a consequence $\Omega_{\text{C IV}}$ starts to decrease, even if at a later time and to a smaller degree than the 'wind' runs.

8 PROBABILITY DISTRIBUTION FUNCTION OF THE C IV DOPPLER PARAMETER

In this Section we focus on the C IV Doppler parameter probability distribution function, plotted at redshift $z = 3$, 2.25 and 1.5 in Figs 13, 14 and 15, respectively. The data from D'Odorico et al. (2010) are also overplotted in these figures with a purple solid line along with the associated Poissonian error (shaded region). For this analysis we considered C IV *lines*.

At redshift $z = 3$ (Fig. 13) all the runs are quite in agreement with the data even if there are some small discrepancies. All the runs tend to underestimate the observed distribution in the first bin, $b_{\text{C IV}} < 4 \, \text{km s}^{-1}$, and slightly overestimate it for $b_{\text{C IV}} > 28 \, \text{km s}^{-1}$. In the intermediate range $4 < b_{\text{C IV}} < 28 \, \text{km s}^{-1}$, the simulations behave differently. The kr37mdw, kr37agn+edw300, kr37co-edw500 (left-hand panel) and sa37edw500 (right-hand panel) runs fit very well the observational data, while runs kr37edw500 and ay37edw500 (right-hand panel) overproduce the observed distribution in the bin centred at $b_{\text{C IV}} = 10 \, \text{km s}^{-1}$. Again runs kr37nf
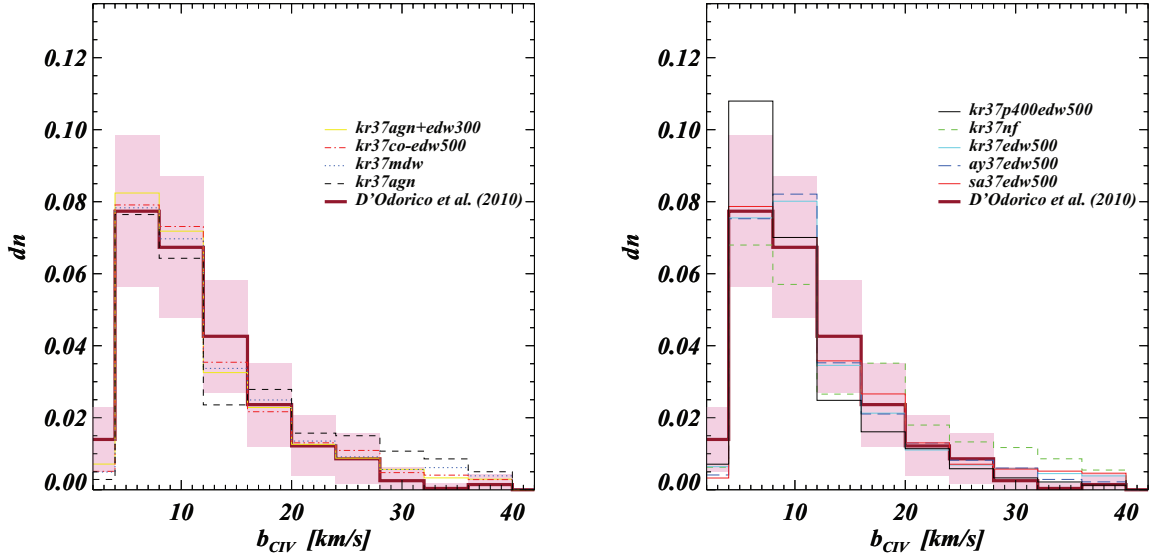
Figure 13. Linewidths $b_{C IV}$ probability distribution function at $z = 3$. Left-hand panel: part I. Right-hand panel: part II. In both panels, data from D'Odorico et al. (2010) are showed by the purple solid line along with the associated Poissonian error (shaded region).
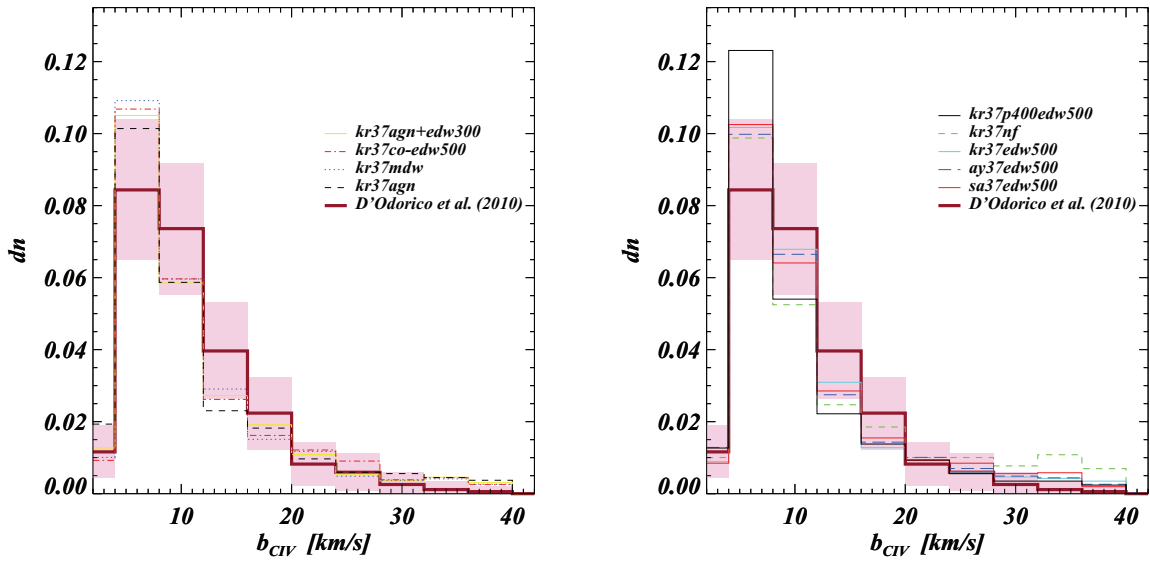

Figure 14. As in Fig. 13, but at redshift $z = 2.25$.

and kr37agn show a different trend with respect to the others, for exactly the same reasons mentioned in the previous sections. Simulations kr37nf (no-feedback; right-hand panel, green dashed line) and kr37agn (AGN feedback; left-hand panel, black dashed line) distributions are shifted towards higher $b_{C IV}$ than the observed one. At this redshift AGN feedback is not active so, as the no-feedback case of kr37nf, the gas remains trapped inside haloes at high density and temperature. Run kr37p400edw500 shows a marked excess of low C IV Doppler parameters due to its improved resolution that can resolve higher densities at earlier times and produces a lot of small metal-enriched clumps in the IGM. At $z = 3$, the median value of the observational Doppler parameters distribution is $9.88 \, \mathrm{km \, s^{-1}}$, while the simulations have median ranging from $8.49 \, \mathrm{km \, s^{-1}}$ (kr37p400edw500) to $13.03 \, \mathrm{km \, s^{-1}}$ (kr37nf).

The situation is different at redshift $z = 2.25$ (Fig. 14) and $z = 1.5$ (Fig. 15). Moving to lower redshift, all the simulations show an excess of low Doppler parameters ($b_{C IV} < 8 \, \mathrm{km \, s^{-1}}$), and also they underproduce the observed distribution in the range $8 < b_{C IV} < 20 \, \mathrm{km \, s^{-1}}$. Moreover, while at low redshift the kr37nf simulation (no-feedback; right-hand panels, green dashed lines) is still shifted towards higher $b_{C IV}$ with respect to the observed distribution, the kr37agn run (AGN feedback; left-hand panels, black dashed lines) at redshift $z = 2.25$ fits better the data and it finally approaches all the other runs at $z = 1.5$, further confirming the increasing efficiency of the AGN feedback at low redshift. At $z = 2.25$ and 1.5, the data by D'Odorico et al. (2010) have median values, respectively, equal to 9.30 and $9.25 \, \mathrm{km \, s^{-1}}$, while the simulations have median around, respectively, 8.55 and
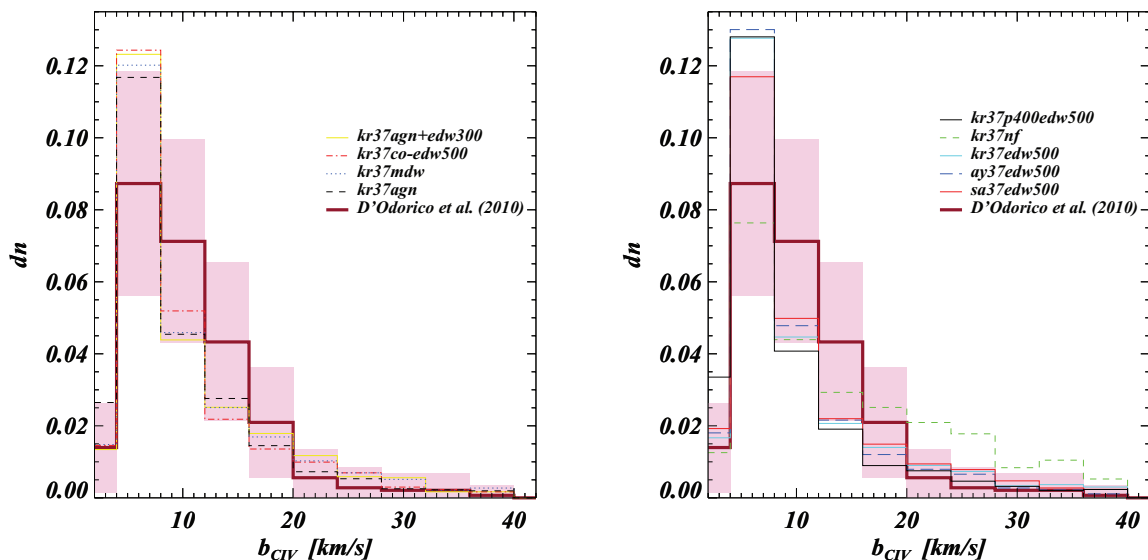
Figure 15. As in Fig. 13, but at redshift $z = 1.5$.

7.40 km s^{-1} (12.47 km s^{-1} in the case of the no-feedback run kr37nf).

We stress that the small discrepancy between observed and simulated distributions for low Doppler parameters ($b_{\rm C\,IV} < 8$ km s^{-1}) appears in a range that is influenced by the adopted resolution (remember that we have convolved the simulated spectra with a Gaussian of 6.6 km s^{-1} FWHM) and a slightly different value than the one used could alleviate this discrepancy.

Compared to that of H I, the C IV Doppler parameter distribution function is less affected by the choice of the UV background (and in particular of the factor of 3.3 discussed in Sections 3 and 5.2). This is due to the fact that C IV absorption is related to higher density regions (mainly the outskirts of galactic haloes) than the H I absorption. In these regions, the impact of the IGM local temperature and density on the ionization state of carbon is considerably more important than the UVB contribution.

9 THE C IV COLUMN DENSITY–DOPPLER PARAMETER RELATION

In Figs 16, 17 and 18, we plot the $b_{\rm C\,IV}$–$N_{\rm C\,IV}$ relation at redshift $z = 3, 2.25$ and 1.5, respectively, for the reference simulations kr37edw500, kr37mdw and kr37agn. The contour plots are colour coded according to the fraction of points that fall in each bin with coordinate ($b_{\rm C\,IV}$, $N_{\rm C\,IV}$). In the upper left-hand panel of the figures, the observational data of D'Odorico et al. (2010) are plotted. As in the previous Section, we considered here C IV lines.

At redshift $z = 3$ (Fig. 16), the data distributions of runs kr37edw500 (EDW) and kr37mdw (MDW) are in agreement with each other but are quite different from the observed one. In particular the simulated distributions are shifted towards higher C IV column densities and are concentrated around a narrower region than the observational data. The low column density tail of the distributions is completely missing, while the high column density tail shows a sort of correlation between the C IV Doppler parameters and $N_{\rm C\,IV}$. We interpret the latter as a T–ρ relation: lines with higher column densities (i.e. associated to denser regions) have higher Doppler parameters (i.e. temperature). The fact that this relation appears only at high column densities is not a surprise: for high values of $N_{\rm C\,IV}$,

absorption lines are very strong and well resolved, so they are good tracers of the physical state of the intergalactic gas and also they are better fitted by VPFIT. The case of run kr37agn is different: in fact the T–ρ relation for large $N_{\rm C\,IV}$ values is missing, while a clump of systems with a large spread in $b_{\rm C\,IV}$ values at low column density is clearly visible. This distribution results because, at redshift $z = 3$, in the kr37agn run the gas resides inside the high-density high-temperature cores of the haloes where it is reprocessed by the stars, and the amount of diffused C IV is rather low (see the right-hand panel of Fig. 12). Therefore, since the C IV absorption lines are weak and not well defined, the quality of the fit made by VPFIT is rather poor. As we reported in Section 5.2, in such a case VPFIT tends to add broad components in order to minimize the χ^2 statistics and this results in the feature of spurious systems at low column density shown in the lower right-hand panel of Fig. 16. While the effect is less evident (but present) for the other runs or in the case of the $b_{\rm H\,I}$–$N_{\rm H\,I}$ relation, it is now much more prominent. Of course, observational data do not present such a feature, because in the 'by eye' procedure of fitting these spurious lines are removed.

At redshift $z = 2.25$ (Fig. 17) and $z = 1.5$ (Fig. 18), the kr37agn run approaches the other two simulations. The $b_{\rm C\,IV}$–$N_{\rm C\,IV}$ correlation at high column densities is now present for all the runs, but the simulated distributions are still different from the observed one. The clump of low-density systems disappears almost completely at $z = 2.25$, but is visible also for runs kr37edw500 and kr37mdw at redshift $z = 1.5$. There is a simple reason for this: at low redshift the amount of C IV, traced by random LOS along the box, decreases (right-hand panel of Fig. 12), while the number of low column density systems significantly increases (Fig. 11) and typically these lines have a large spread in their Doppler parameter value.

The difference between simulated and observed distributions could also be due to the fact that simulated haloes, and in particular their outskirts, can have different properties from that of the observed ones: for example this is also seen from the Si II statistics in DLA systems that appear to be in disagreement with the observations. Although in this paper we explore the effect of feedback, there might be other physical effects that can contribute as well in shaping the properties of the $b_{\rm C\,IV}$–$N_{\rm C\,IV}$ distribution.
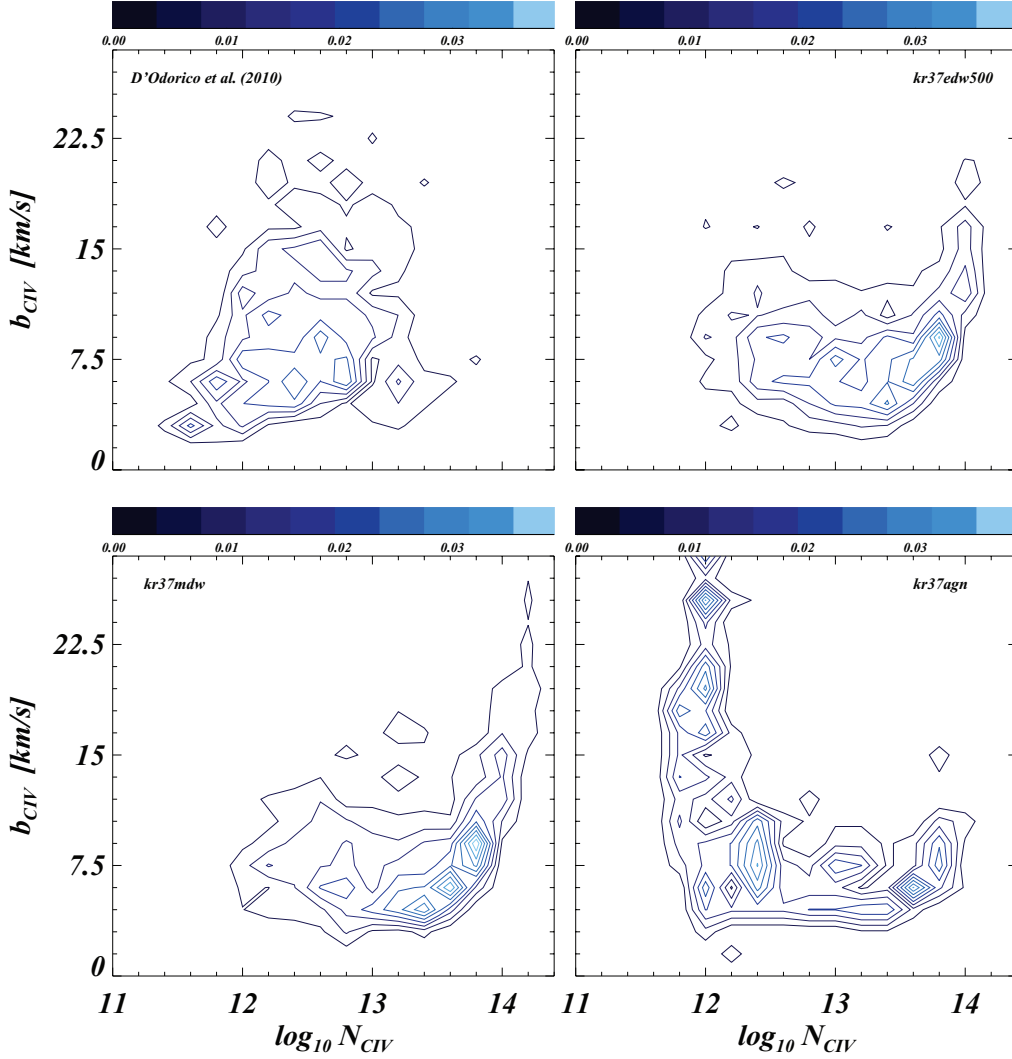
Figure 16. $b_{C\,IV}$–$N_{C\,IV}$ relation at $z = 3$. The horizontal bars are colour coded according to the fraction of points that fall in each bin with coordinate ($b_{C\,IV}$, $N_{C\,IV}$). Upper left-hand panel: observational data from D'Odorico et al. (2010).

10 $N_{C\,IV}$–$N_{H\,I}$ CORRELATED ABSORPTION

The last part of this work is dedicated to the H I–C IV correlated absorption. We define as correlated absorption H I–C IV systems in which C IV and H I are physically dependent or, in other words, related to the same absorptive structure. In real spectra, however, two absorbers each containing C IV could be very close in redshift space but far in real space due to the bulk motions and the peculiar velocity. For this reason there are often serious problems on how to associate each C IV components to physically corresponding H I components. In this Section, besides the data of D'Odorico et al. (2010), we compare with the fitting formulae obtained from the Kim et al. (2010) data. In order to do that, only for this analysis we changed the velocity range, dv_{min}, used so far to define *systems* of lines. Following Kim et al. (2010) and differently from what was done in Sections 6 and 7, where we set $dv_{min} = 50\,\text{km s}^{-1}$, we use here the velocity interval $[-250\,\text{km s}^{-1}, 250\,\text{km s}^{-1}]$ both for the simulated and the observed C IV and H I systems.

In Figs 19 and 20 we show our findings for some of the simulations in Table 2 and for the D'Odorico et al. (2010) data. The red dashed and yellow solid curves represent the Kim et al. (2010) fit,

obtained by using the function

$$\log N_{C\,IV} = \left[\frac{C_1}{\log N_{H\,I} + C_2} \right] + C_3. \tag{20}$$

The parameters for the red dashed curves are $C_1 = [-4.43 \pm 1.30, -7.57 \pm 1.80]$, $C_2 = [-13.04 \pm 0.44, -12.45 \pm 0.45]$ and $C_3 = [15.22 \pm 0.17, 15.65 \pm 0.19]$ at $z = [2.25, 3.0]$. These red dashed curves represent a fit to *all* the Kim et al. (2010) data available at the two different redshift. The parameters for the yellow solid curves are $C_1 = [-2.01 \pm 0.35, -2.51 \pm 0.47]$, $C_2 = [-14.22 \pm 0.14, -14.08 \pm 0.20]$ and $C_3 = [14.96 \pm 0.05, 15.09 \pm 0.07]$ at $z = [2.25, 3.0]$. These curves represent an improved fit made to reproduce better the clump of systems at low $N_{H\,I}$ and low $N_{C\,IV}$.

At redshift $z = 3$ (Fig. 19) for the D'Odorico et al. (2010) observational data and for the kr37agn+edw300, kr37edw500 and kr37mdw runs, the bulk of systems is located at $\log N_{H\,I}\,(\text{cm}^{-2}) < 16$ and it follows the Kim et al. (2010) fitting functions, even if with a slightly steeper trend, while at $\log N_{H\,I}\,(\text{cm}^{-2}) > 16$ the spread in the simulated data increases [also the data of Kim et al. (2010) present a sort of bimodality with high H I column density distribution more spread than the tight low H I column density one]. Runs
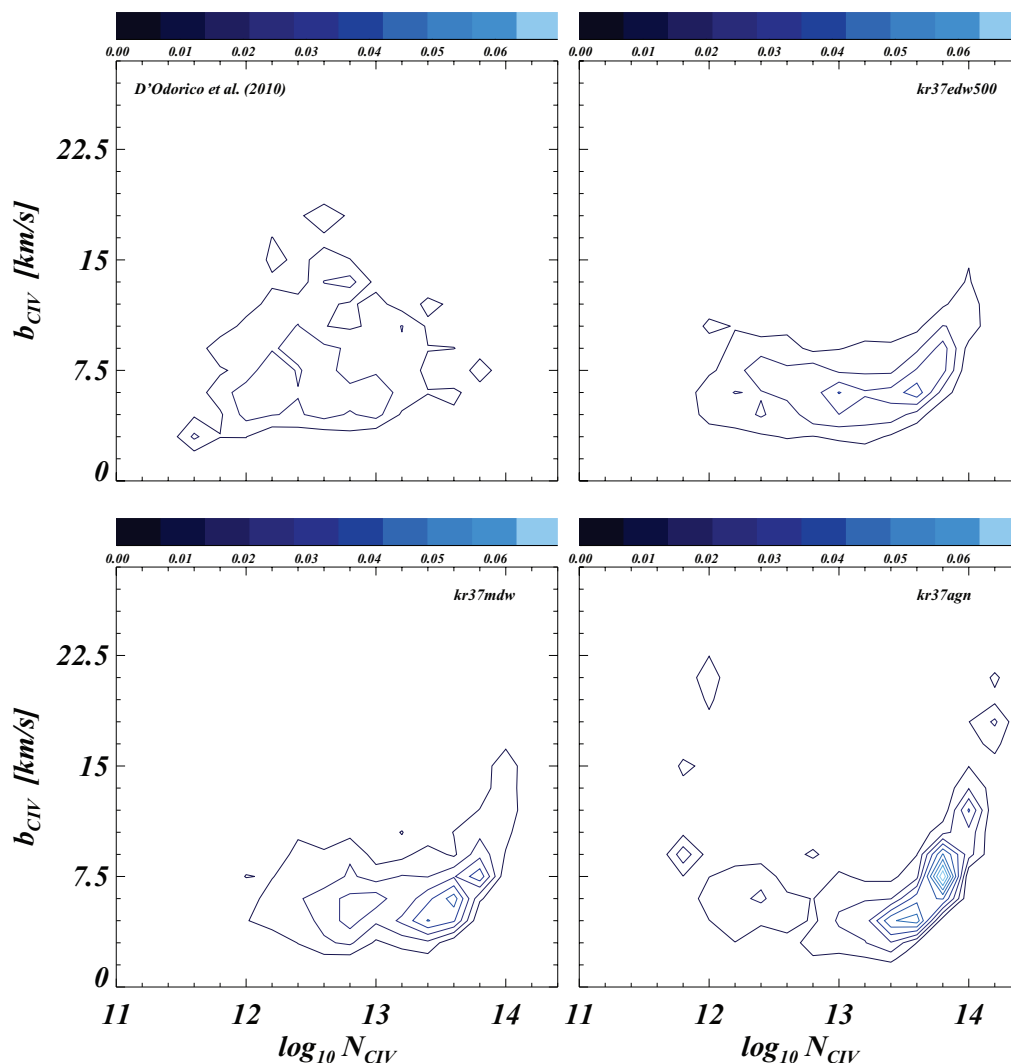
Figure 17. As in Fig. 16, but at redshift $z = 2.25$.

kr37nf (no-feedback) and kr37agn (AGN feedback) at this redshift behave similarly: they do not show the $\log N_{\rm HI}$ (cm^{-2}) < 16 C IV–H I correlation above, and the $\log N_{\rm HI}$ (cm^{-2}) > 16 systems are rare. All the simulations show a strip of values with $\log N_{\rm HI}$ (cm^{-2}) < 15 and $\log N_{\rm CIV}$ (cm^{-2}) ~ 12. This is due to the VPFIT spurious line-fitting effect described in the previous Section. In fact, it is particularly evident for runs kr37nf and kr37agn, because in these two cases the amount of the diffuse C IV is lower and the C IV absorption lines are weak and not well defined.

At redshift $z = 2.25$ (Fig. 20), the above trends are in place even if all the simulated distributions are now shifted towards slightly lower H I column densities with respect to the fitting functions of Kim et al. (2010). Otherwise, the number of components of the D'Odorico et al. (2010) data increases at this redshift and the bulk of systems at $\log N_{\rm HI}$ (cm^{-2}) < 16 is well fitted by the functions of Kim et al. (2010). Again, moving to lower redshift, the simulation with AGN feedback, kr37agn, starts to follow the other wind runs.

To summarize, two effects are visible from the plots: (i) for a given $N_{\rm HI}$, the scatter in the corresponding $N_{\rm CIV}$ is broader, and the $N_{\rm CIV}$ values typically larger, than what is inferred from observations; (ii) the simulated distributions of $N_{\rm HI}$ are slightly lower compared

to the Kim et al. (2010) fitting functions and the D'Odorico et al. (2010) data at redshift $z = 2.25$.

11 CONCLUSIONS AND DISCUSSION

In this paper, we investigated the global properties of triply ionized carbon (C IV) as an IGM tracer at $z \geq 1.5$. From the numerical point of view, we presented the results of a new set of hydrodynamic simulations that incorporate feedback either in the form of galactic winds or in the form of energy from BH accretion (AGN feedback). From the observational point of view, we relied on recent high-resolution data sets obtained with the UVES spectrograph at VLT and the HIRES spectrograph at Keck. The main results can be summarized as follows:

(i) The statistics of H I are weakly affected by the feedback prescription implemented: both the CDDF and the Doppler width distributions do not change significantly when considering the different simulations. We regard this as a geometrical effect: winds and AGN feedback are stronger at the intersection of IGM filaments and these sites have usually small filling factor. Only the high column
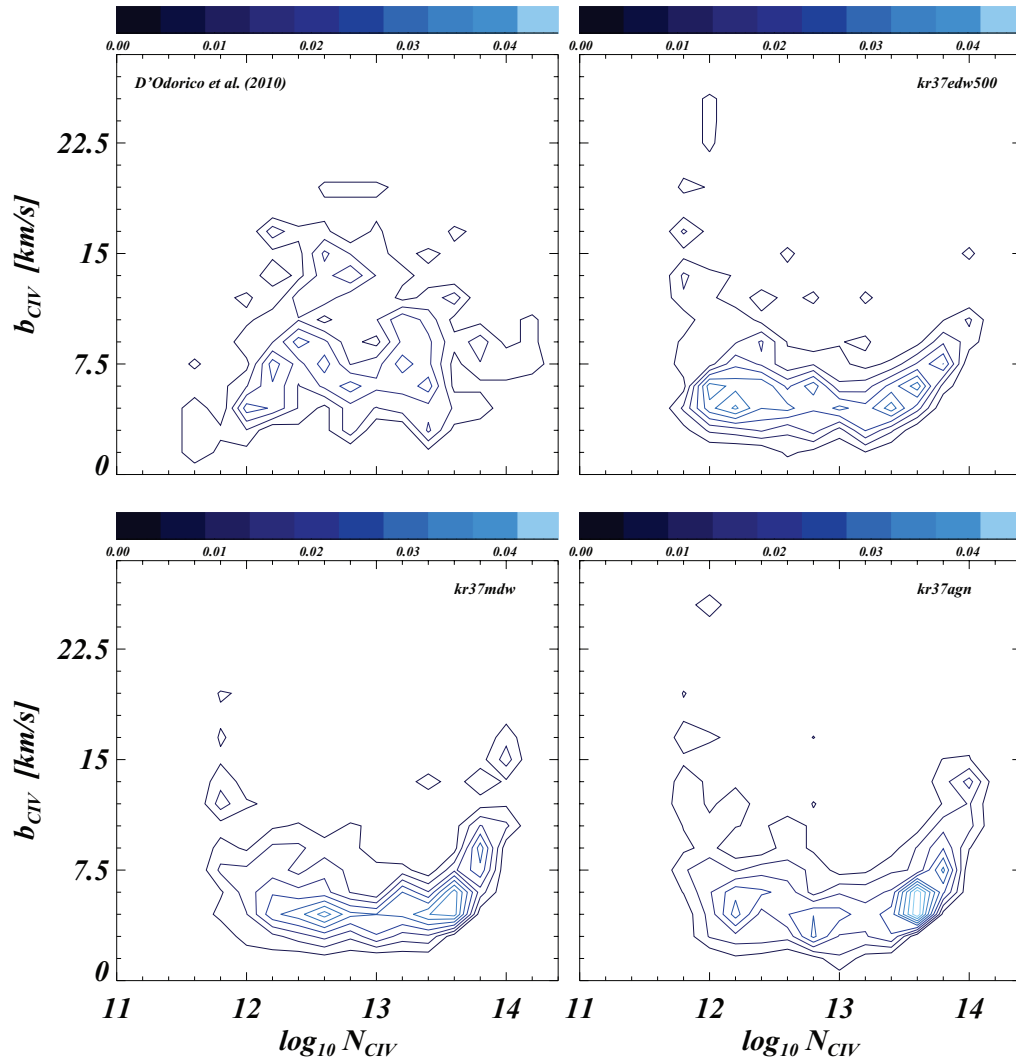
Figure 18. As in Fig. 16, but at redshift $z = 1.5$.

density tail shows small differences between the runs considered (Section 5). The fact that overall our simulations reproduce well all the H I statistics confirms that we are catching the physics of the gas traced by the neutral hydrogen. The remaining small discrepancies with the observational data could be due to the UV background we used (Haardt & Madau 1996; produced by quasars and galaxies, with the heating rates multiplied by a factor of 3.3), that heats the gas too much. In minor part, the discrepancies are also due to a numerical effect introduced by the line-fitting software VPFIT.

(ii) Compared to that of H I, the statistics of C IV is strongly affected by feedback. If we consider *systems* of lines as defined in Section 2, at redshift $z = 3$, 2.25 and 1.5, all the simulations except for the no-feedback run kr37nf and the AGN feedback run kr37agn (the latter only at high redshift) agree with the observed C IV CDDF. Galactic wind feedback starts to be active at high redshift, but moving to lower redshift, also the AGN feedback becomes effective and the kr37agn simulation follows all the other wind runs (see Figs 9, 10 and 11).

(iii) In the second part of Section 7, we presented the evolution with redshift of the C IV cosmological mass density, calculated considering the CDDF of the C IV absorption lines. In the redshift range

$z = 2.5$–3.5, our simulations, except for the no-feedback run kr37nf and the AGN feedback run kr37agn, reproduce the observed $\Omega_{C IV}(z)$ evolution, even if with a slight overestimation, and they perfectly reproduce the observational data around redshift $z = 2.25 \pm 0.25$. At lower redshift we found a decreasing trend at variance with the increasing trend shown by the observational data (right-hand panel of Fig. 12). In the AGN case, the trend is nearly constant at low redshift and in better agreement with data. We think that a better calibration of the coupled AGN + galactic wind feedback model of run kr37agn+edw300 could help to improve this result.

(iv) At all the redshift considered, the C IV Doppler parameter distribution is in good agreement with the observational data. The no-feedback and AGN feedback simulations (the latter only at high redshift) result in distributions shifted towards higher $b_{C IV}$ than the observed ones: this is due to the fact that these runs produce gas around galaxies that is too hot than what was inferred from observations (Section 8).

(v) The overall $b_{C IV}$–$N_{C IV}$ data distribution of our reference simulations is different from the observed one. The high column density tail of all the runs considered (but for the AGN feedback run, this is true only at low redshift) shows a sort of correlation between the C IV
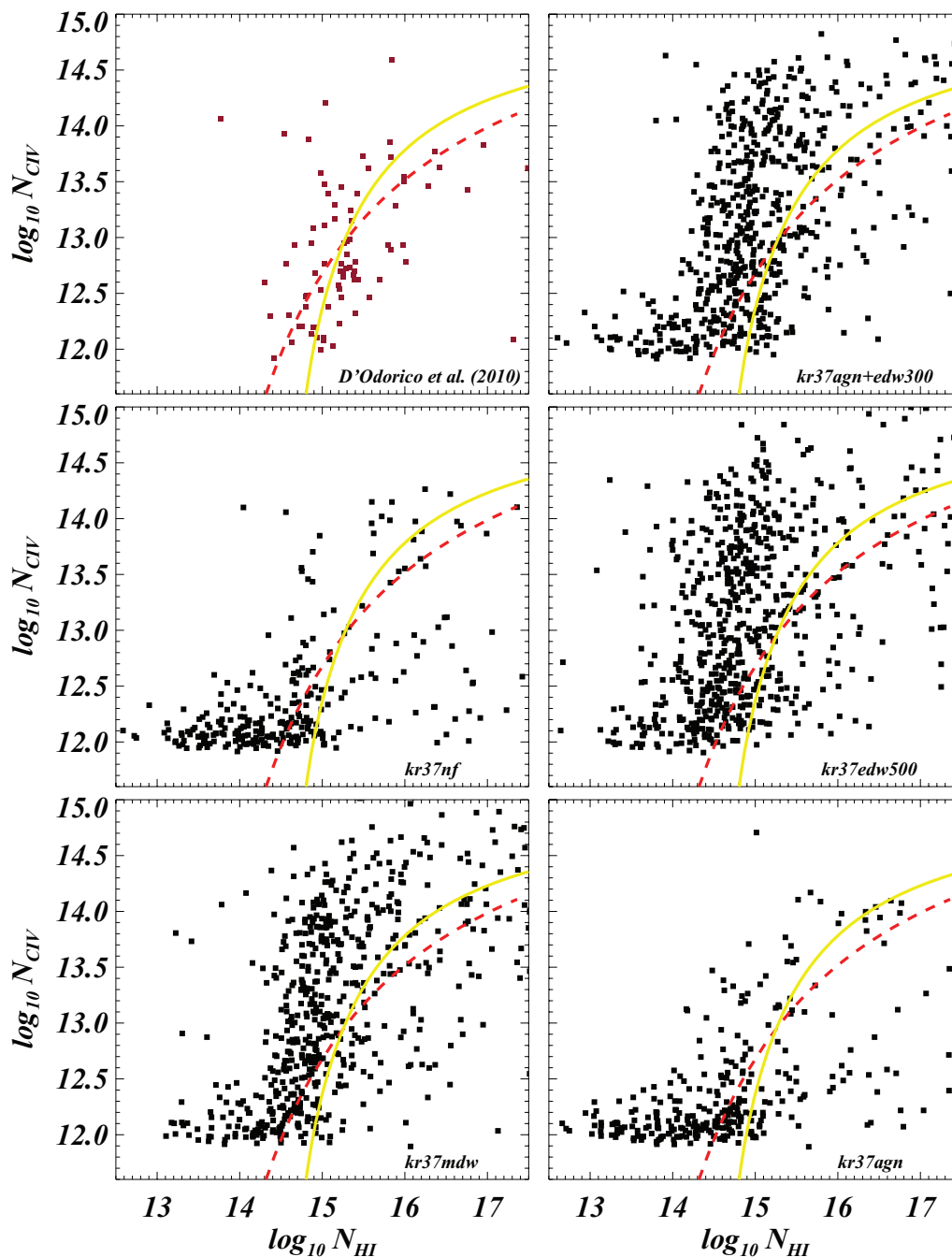
Figure 19. Column densities $N_{C IV}$–$N_{H I}$ correlated absorption for systems at $z = 3$. Upper left-hand panel: observational data from D'Odorico et al. (2010). The red dashed and yellow solid curves represent the fitting functions of Kim et al. (2010).

Doppler parameters and the column density, in which the Doppler parameters increase as $N_{C IV}$ increases: the sign of a well-defined temperature–density relation for the high density gas. Especially at low redshift, when the amount of C IV traced by random LOS along the box decreases, a clump of systems with a huge scatter in the $b_{C IV}$ values at low C IV column density is present. This effect should be regarded as of numerical origin and it is introduced by VPFIT when fitting regions close to the continuum in the mock data set (Section 9). A more careful comparison between data and simulations is needed in order to address this effect at a more quantitative level.

(vi) In Section 10 we explored the correlated C IV–H I absorption, considering *systems* of lines in which C IV and H I are physically dependent. At the two redshift considered, $z = 3$ and 2.25, both our reference runs and the observational data of D'Odorico et al. (2010) roughly follow the fit proposed by Kim et al. (2010), even if the simulations show a slightly steeper trend in the range $\log N_{H I}$ $(\text{cm}^{-2}) < 16$.

(vii) Even if we are not able to fit all the statistics at once if we consider the neutral hydrogen H I and the triply ionized carbon C IV, MDW simulation reproduces best all the different quantities
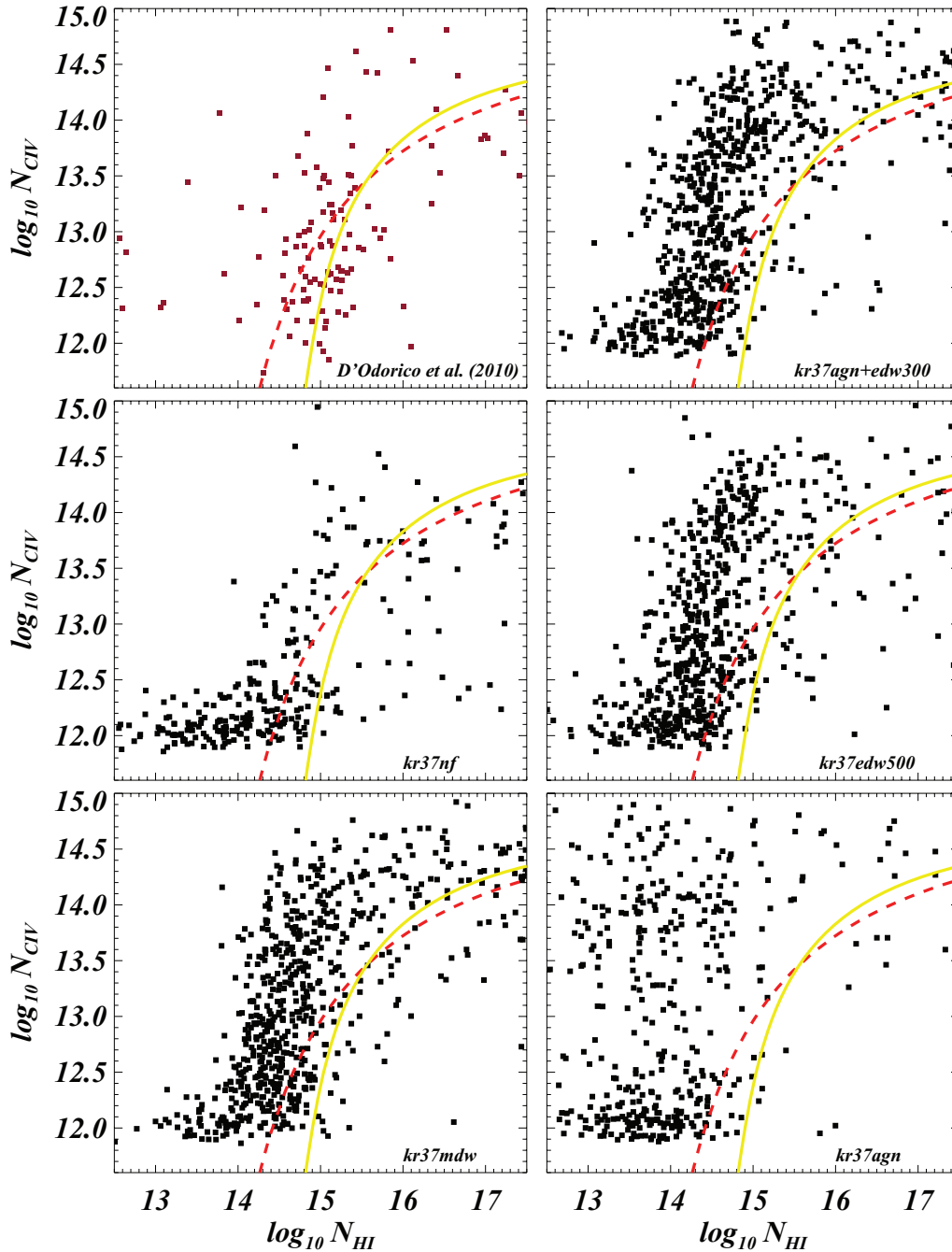
Figure 20. As in Fig. 19, but at redshift $z = 2.25$.

explored in this paper [as found for Damped Lyman α systems by Tescari et al. (2009), and for IGM metal lines by Oppenheimer & Davé (2006, 2008)].

(viii) To sum up, feedback appears to be a crucial physical ingredient in order to reproduce statistics of metal absorption lines. In particular, the effect of galactic winds triggered by supernovae is important at high redshift, while the effect of BH accretion feedback starts to become prominent at $z < 3$. However, because the AGN feedback is very strong, it will be crucial to improve the coupled AGN + galactic wind model, where the effect of the winds at high redshift reduces the strength of the BH accretion at low redshift.

In our analysis, we found two different effects biasing the statistics related to the H I and C IV absorption lines: the choice of the UV background and the VPFIT lines-fitting procedure. In the future, we will try to improve these statistics by using a more physically motivated UV background that takes into account He II reionization at $z \sim 3$. Furthermore, we will try to improve our automatic line-fitting analysis by removing numerical artefacts introduced by VPFIT, since the automatic fitting procedure is not likely to be as accurate as a 'by eye' fitting made by an observer, and introduce spurious lines especially in the continuum region. Our results can also be tested by using other statistics based on pixel optical depths techniques.

A second possible improvement of the results presented in this paper is the refinement of the feedback models and the inclusion of new physical processes like turbulence, metal diffusion and radiative transfer that can help in polluting, with metals, the low-density IGM. So far we explored feedback prescriptions in the form of energy-driven glactic winds (EDW), momentum-driven galactic winds (MDW) and BH accretion (AGN feedback). Exploring the combined effect of these models seems to be promising: for example the 'energy coupled MDW' model by Choi & Nagamine (2010) succeeds in enriching the gas (like the EDW model) without heating too much the IGM (like the MDW model). The modellization inside the hydrodynamic simulations of the radiative transfer is fundamental and could also impact on the metal mixing. Finally, it will be crucial to incorporate in the GADGET-2 code the small-scale turbulence and its impact on the metal diffusion at large scales. With physical mixing, fluid elements on a fixed (resolved) physical scale do exchange energy/entropy due to unresolved (turbulent) motions: diffusion allows some ejecta gas to mix while exiting the galaxies (Shen, Wadsley & Stinson 2009). All the previous effects, once included in simulations, could help in improving our understanding of the chemical and physical evolution of the IGM and provide a more comprehensive framework of the high-redshift galaxy/IGM interplay.

REFERENCES

Adelberger K. L., Shapley A. E., Steidel C. C., Pettini M., Erb D. K., Reddy N. A., 2005, ApJ, 629, 636
Aguirre A., Schaye J., Hernquist L., Kay S., Springel V., Theuns T., 2005, ApJ, 620, L13
Aracil B., Petitjean P., Pichon C., Bergeron J., 2004, A&A, 419, 811
Arimoto N., Yoshii Y., 1987, A&A, 173, 23
Asplund M., Grevesse N., Sauval A. J., 2005, in Barnes T. G., III, Bash F. N., eds, ASP Conf. Ser. Vol. 336, Cosmic Abundances as Records of Stellar Evolution and Nucleosynthesis. Astron. Soc. Pac., San Francisco, p. 25
Becker G. D., Rauch M., Sargent W. L. W., 2009, ApJ, 698, 1010
Bergeron J. et al., 2004, Messenger, 118, 40
Bertone S., Schaye J., Booth C. M., Dalla Vecchia C., Theuns T., Wiersma R. P. C., 2010a, 408, 1120
Bertone S., Schaye J., Dalla Vecchia C., Booth C. M., Theuns T., Wiersma R. P. C., 2010b, MNRAS, 407, 544
Boksenberg A., Sargent W. L. W., Rauch M., 2003, ApJS, preprint (astro-ph/0307557v1)
Bolton J. S., Haehnelt M. G., 2007, MNRAS, 374, 493
Bolton J. S., Haehnelt M. G., Viel M., Springel V., 2005, MNRAS, 357, 1178
Bondi H., 1952, MNRAS, 112, 195
Booth C. M., Schaye J., 2009, MNRAS, 398, 53
Calura F., Matteucci F., 2006, MNRAS, 369, 465
Calura F., Menci N., 2009, MNRAS, 400, 1347
Cen R., Chisari N. E., 2010, ApJ, preprint (arXiv:1005.1451)

Cen R., Nagamine K., Ostriker J. P., 2005, ApJ, 635, 86
Choi J., Nagamine K., 2010, MNRAS, doi:10.1111/j.1365-2966.2010.17632.x
Cowie L. L., Songaila A., Kim T., Hu E. M., 1995, AJ, 109, 1522
Dalla Vecchia C., Schaye J., 2008, MNRAS, 387, 1431
Davé R., Oppenheimer B. D., Katz N., Kollmeier J. A., Weinberg D. H., 2010, ArXiv e-prints
Dekker H., D'Odorico S., Kaufer A., Delabre B., Kotzlowski H., 2000, in Iye M., Moorwood A. F. eds, Proc. SPIE Conf. Ser. Vol. 4008, Optical and IR Telescope Instrumentation and Detectors. p. 534
Di Matteo T., Springel V., Hernquist L., 2005, Nat, 433, 604
Di Matteo T., Colberg J., Springel V., Hernquist L., Sijacki D., 2008, ApJ, 676, 33
D'Odorico V., Petitjean P., Cristiani S., 2002, A&A, 390, 13
D'Odorico V., Bruscoli M., Saitta F., Fontanot F., Viel M., Cristiani S., Monaco P., 2008, MNRAS, 389, 1727
D'Odorico V., Calura F., Cristiani S., Viel M., 2010, MNRAS, 401, 2715
Fabjan D., Borgani S., Tornatore L., Saro A., Murante G., Dolag K., 2010, MNRAS, 401, 1670
Faucher-Giguère C.-A., Lidz A., Hernquist L., Zaldarriaga M., 2008, ApJ, 688, 85
Ferland G. J., Korista K. T., Verner D. A., Ferguson J. W., Kingdon J. B., Verner E. M., 1998, PASP, 110, 761
Fontana A., Ballester P., 1995, Messenger, 80, 37
Haardt F., Madau P., 1996, ApJ, 461, 20
Haehnelt M. G., Steinmetz M., Rauch M., 1996, ApJ, 465, L95
Katz N., Weinberg D. H., Hernquist L., 1996, ApJS, 105, 19
Kawata D., Rauch M., 2007, ApJ, 663, 38
Kim T., Bolton J. S., Viel M., Haehnelt M. G., Carswell R. F., 2007, MNRAS, 382, 1657
Kim T.-S., Partl A. M., Carswell R. F., Mücket J. 2010, MNRAS, submitted
Kirkman D., Tytler D., 1997, ApJ, 484, 672
Kobayashi C., Springel V., White S. D. M., 2007, MNRAS, 376, 1465
Komatsu E. et al., 2009, ApJS, 180, 330
Kroupa P., 2001, MNRAS, 322, 231
Lesgourgues J., Viel M., Haehnelt M. G., Massey R., 2007, J. Cosmology Astroparticle Phys., 11, 8
Martin C. L., 2005, ApJ, 621, 227
Murray N., Quataert E., Thompson T. A., 2005, ApJ, 618, 569
Nagamine K., Springel V., Hernquist L., 2004, MNRAS, 348, 435
Oppenheimer B. D., Davé R., 2006, MNRAS, 373, 1265
Oppenheimer B. D., Davé R., 2008, MNRAS, 387, 577
Oppenheimer B. D., Davé R., Finlator K., 2009, MNRAS, 396, 729
Padovani P., Matteucci F., 1993, ApJ, 416, 26
Pichon C., Scannapieco E., Aracil B., Petitjean P., Aubert D., Bergeron J., Colombi S., 2003, ApJ, 597, L97
Pieri M. M., Schaye J., Aguirre A., 2006, ApJ, 638, 45
Porciani C., Madau P., 2005, ApJ, 625, L43
Ricotti M., Gnedin N. Y., Shull J. M., 2000, ApJ, 534, 41
Rupke D. S., Veilleux S., Sanders D. B., 2005, ApJS, 160, 115
Ryan-Weber E. V., Pettini M., Madau P., 2006, MNRAS, 371, L78
Ryan-Weber E. V., Pettini M., Madau P., Zych B. J., 2009, MNRAS, 395, 1476
Saitta F., D'Odorico V., Bruscoli M., Cristiani S., Monaco P., Viel M., 2008, MNRAS, 385, 519
Salpeter E. E., 1955, ApJ, 121, 161
Scannapieco E., Pichon C., Aracil B., Petitjean P., Thacker R. J., Pogosyan D., Bergeron J., Couchman H. M. P., 2006, MNRAS, 365, 615
Schaerer D., 2003, A&A, 397, 527
Schaye J., 2001, ApJ, 559, 507
Schaye J., Rauch M., Sargent W. L. W., Kim T., 2000a, ApJ, 541, L1
Schaye J., Theuns T., Rauch M., Efstathiou G., Sargent W. L. W., 2000b, MNRAS, 318, 817
Schaye J., Aguirre A., Kim T.-S., Theuns T., Rauch M., Sargent W. L. W., 2003, ApJ, 596, 768
Seljak U., Zaldarriaga M., 1996, ApJ, 469, 437
Shakura N. I., Sunyaev R. A., 1973, A&A, 24, 337
Shen S., Wadsley J., Stinson G., 2010, MNRAS, 407, 1581

Sijacki D., Pfrommer C., Springel V., Enßlin T. A., 2008, MNRAS, 387, 1403

Simcoe R. A., Sargent W. L. W., Rauch M., Becker G., 2006, ApJ, 637, 648

Sommer-Larsen J., Fynbo J. P. U., 2008, MNRAS, 385, 3

Springel V., 2005, MNRAS, 364, 1105

Springel V., Hernquist L., 2003, MNRAS, 339, 289

Springel V., Di Matteo T., Hernquist L., 2005, MNRAS, 361, 776

Steidel C. C., Erb D. K., Shapley A. E., Pettini M., Reddy N., Bogosavljević M., Rudie G. C., Rakic O., 2010, ApJ, 717, 289

Storrie-Lombardi L. J., McMahon R. G., Irwin M. J., 1996, MNRAS, 283, L79

Sutherland R. S., Dopita M. A., 1993, ApJS, 88, 253

Tescari E., Viel M., Tornatore L., Borgani S., 2009, MNRAS, 397, 411

Theuns T., Leonard A., Efstathiou G., Pearce F. R., Thomas P. A., 1998, MNRAS, 301, 478

Theuns T., Viel M., Kay S., Schaye J., Carswell R. F., Tzanavaris P., 2002, ApJ, 578, L5

Thielemann F.-K. et al., 2003, Nuclear Phys. A, 718, 139

Tornatore L., Borgani S., Dolag K., Matteucci F., 2007, MNRAS, 382, 1050

Tornatore L., Borgani S., Viel M., Springel V., 2010, MNRAS, 402, 1911

Tytler D. et al., 2009, MNRAS, 392, 1539

van den Hoek L. B., Groenewegen M. A. T., 1997, A&AS, 123, 305

Vikhlinin A. et al., 2009, ApJ, 692, 1060

Weymann R. J., Carswell R. F., Smith M. G., 1981, ARA&A, 19, 41

Wiersma R. P. C., Schaye J., Theuns T., Dalla Vecchia C., Tornatore L., 2009, MNRAS, 399, 574

Wiersma R. P. C., Schaye J., Dalla Vecchia C., Booth C. M., Theuns T., Aguirre A., 2010, MNRAS, 409, 132

Woosley S. E., Weaver T. A., 1995, ApJS, 101, 181

This paper has been typeset from a TeX/LaTeX file prepared by the author.